Anomalous Doppler Effect in Superfluid and Supersolid Atomic Gases

Tomasz Zawiślak[1], Marija Šindik[1,2] Sandro Stringari[1], and Alessio Recati[1,*]

[1]*Pitaevskii BEC Center, CNR-INO and Dipartimento di Fisica, Università di Trento, Via Sommarive 14, 38123 Povo, Trento, Italy*
[2]*Institute of Physics Belgrade, University of Belgrade, Pregrevica 118, 11080 Belgrade, Serbia*

By employing the formalism of hydrodynamics, we derive novel analytic predictions for the Doppler effect in superfluids with broken Galilean invariance and hosting persistent currents at zero temperature. We consider two scenarios: when Galilean invariance is broken explicitly (by external potentials) and spontaneously, as it happens in a supersolid. In the former case, the presence of a stationary current affects the propagation of sound via an anomalous Doppler term proportional to the density derivative of the superfluid fraction. In supersolids, where, according to Goldstone theorem, distinct sounds of hybrid superfluid and crystal nature can propagate, the Doppler effect can be very different for each sound. Quantitative estimates of the Doppler shifts are obtained for Bose-Einstein condensed atomic gases, described by Gross-Pitaevskii theory. The estimates are obtained both calculating the thermodynamic parameters entering the hydrodynamic results and from full time-dependent simulations.

In a classical fluid moving at a small velocity v_f, the sound speed c_0 is modified by the kinematic Doppler shift as $c = c_0 \pm v_f$, depending on whether the sound propagates parallel $(+)$ or antiparallel $(-)$ to the velocity v_f. The Doppler effect has been predicted to be different in a superfluid due to the relative velocity between the normal and the superfluid component.

This problem was first addressed a long time ago by Khalatnikov [1] for superfluid helium at finite temperature, where the motion of the liquid is described by Landau's two-fluid hydrodynamics. Stimulated by early experimental results on the Doppler effect in the propagation of fourth sound in helium [2], further theoretical studies have pointed out the occurrence of nontrivial, anomalous Doppler shifts in ^{4}He [3–5], ^{4}He-^{3}He mixture [6], as well as in superfluid ^{3}He [7]. To our knowledge, however, a clear experimental confirmation of the anomalous Doppler effect in liquid helium is still missing.

In this Letter, we demonstrate the possibility of a zero-temperature Doppler effect in ultracold gas superfluids [8–10], which, different from liquid helium, allow for a microscopic treatment based on Gross-Pitaevskii theory. We focus on density-modulated configurations, where the superfluid density can differ significantly from the average density even at zero temperature. Density-modulated phases in ultracold atomic gases can be the result of an external periodic potential (optical lattices [11]) or of the spontaneous breaking of translational symmetry, yielding supersolidity [12]. The propagation of sound and the occurrence of collective oscillations, in the absence of

steady currents, have already been the subject of experimental investigations in both cases (see [13–15] and [16–18], respectively). Furthermore, the Doppler effect was observed in a uniform Bose-Einstein condensed gas confined in a ring, where it was used to measure the quanta of circulation characterizing the velocity of the superfluid flow [19].

In the presence of an external periodic potential, the normal component of the fluid is locked, and only the superfluid component can move. Instead, in supersolid configurations, both superfluid and normal (crystal) components can move. As predicted in the seminal paper by Andreev and Lifshitz [20], Goldstone modes of hybridized crystalline and superfluid nature are expected to occur in a supersolid (see also [21]). These modes are expected to react differently to the presence of a relative motion between the two components.

We provide general analytical results for Doppler shifts at zero temperature within a hydrodynamic approach, which, in the case of a supersolid, have never been obtained before. Considering ultracold gas platforms, we use Gross-Pitaevskii theory to confirm the validity of the hydrodynamic predictions and to determine the parameters entering the hydrodynamic equations. In particular, concerning supersolids, we consider the dipolar gas platform [22–26] (see also [12] and references therein).

In the following, for the sake of simplicity, we consider a linear tube geometry of length L, with periodic boundary conditions, where we can use one-dimensional hydrodynamic theories. In cold atomic gases, quasi-one-dimensional configurations hosting permanent currents can be experimentally realized using ring-shaped trapping potentials with sufficiently large radii.

---

*Contact author: alessio.recati@ino.cnr.it

Doppler shift of fourth sound—One peculiar sound that propagates in superfluid helium occurs when the normal component is at rest due to viscous drag in porous media [27] or in a narrow channel [28]. This mode is usually referred to as fourth sound. An analog mode—hereafter also called fourth sound—propagates at low temperature in a Bose-Einstein condensed atomic gas in the presence of a periodic external potential, which causes the pinning of the normal component.

Doppler effect in fourth sound was observed in helium in a superleak [2,29]. In these pioneering experimental works, it was suggested that the Doppler shift has a kinematic nature and is fixed by the fluid velocity $v_f = v_s \rho_s / \rho$, given by the current divided by the mass density ρ, with ρ_s and v_s the superfluid density and the superfluid velocity, respectively. However, a more detailed analysis based on two-fluid hydrodynamics showed that this prediction is, in general, not correct [5]. The correct result for the Doppler effect of fourth sound at zero temperature can be derived within the Hamiltonian formalism for two-fluid hydrodynamics [30]. Assuming that the stationary superfluid velocity is small, the energy density of the system, in the frame where the normal component is at rest, is given by the expansion $\epsilon(\rho, v_s) = \epsilon_0(\rho) + (1/2)\rho_s v_s^2$, where ϵ_0 is the energy at rest. The superfluid velocity is irrotational and can be written as $v_s = \hbar \partial_x \phi / m$, where the macroscopic phase ϕ is canonically conjugated to the density [31]. The Hamiltonian equations of motion for ρ and v_s then take the form of the following (collisionless) hydrodynamic (HD) equations:

$$\partial_t \rho + \partial_x (\rho_s v_s) = 0, \qquad (1)$$

$$\partial_t v_s + \partial_x \left(\mu_0 + \frac{1}{2} \frac{\partial \rho_s}{\partial \rho} v_s^2 \right) = 0, \qquad (2)$$

where $\mu_0(\rho) = \partial \epsilon_0 / \partial \rho$ is the chemical potential calculated at $v_s = 0$. The two HD equations correspond to the atom number conservation and to the presence of superfluid long-range order.

Sound propagation—corresponding to the superfluid Goldstone mode—is described by linearizing the above equations around the uniform equilibrium values ρ_0, ρ_s^0, and v_s^0, as $\rho(x,t) = \rho_0 + \delta\rho(x,t)$, $\rho_s(x,t) = \rho_s^0 + (\partial \rho_s / \partial \rho) \delta\rho(x,t)$, and $v_s(x,t) = v_s^0 + \delta v_s(x,t)$. In this way, we find that the excitations obey the phononic dispersion relation $\omega(q) = c|q|$, with q the wave vector of the sound wave and c the speed of sound. The latter is given by $c^\pm = c_0 \pm \Delta c$, where $c_0 = \sqrt{f_s \kappa^{-1}}$ is the zero-temperature value of the fourth sound velocity in the absence of current, with $f_s = \rho_s / \rho$ the superfluid fraction and $\kappa^{-1} = \rho \partial_\rho \mu_0$ the inverse compressibility [32]. Finally, the Doppler shift reads

$$\Delta c = \frac{\partial \rho_s}{\partial \rho} v_s^0 = \left(f_s + \rho \frac{\partial f_s}{\partial \rho} \right) v_s^0. \qquad (3)$$

Therefore, due to the density dependence of the superfluid fraction, the Doppler shift differs, in general, from the kinematic expectation $f_s v_s^0$. The expressions given by Eqs. (1)–(3) hold at zero temperature for both Bose and Fermi superfluids, provided the superfluid velocity is small enough, namely, $v_s^0 \ll c_0$. Similar results were obtained in [3] in the case of superleak helium configurations, with special focus on finite size effects, and in [33,34] in the case of atomic Bose-Einstein condensates in optical lattices, after linearization of the time-dependent Gross-Pitaevskii equation (GPE). The superfluid fraction in these latter works has to be interpreted in terms of effective tunneling or effective mass.

The result of Eq. (3) can be easily generalized to the case of an optical lattice moving with velocity v_n^0, by a simple Galilean transformation, i.e., $\Delta c = v_n^0 + (\partial \rho_s / \partial \rho)(v_s^0 - v_n^0) = (\partial \rho_s / \partial \rho) v_s^0 + (\partial \rho_n / \partial \rho) v_n^0$, with $\rho_n = \rho - \rho_s$ the normal density, thereby revealing that anomalous Doppler shifts take place only if the two fluids move with different velocities.

We verify the validity of the hydrodynamic result (3), when applied to a Bose-Einstein condensed gas, by numerically solving the time-dependent GPE in the presence of an optical lattice. The two approaches are expected to be consistent in the phonon long wavelength limit. We consider realistic parameters for a gas of $N = 2 \times 10^5$ ^{87}Rb atoms confined in a tube of length $L = 96$ μm along the x axis, subject to periodic boundary conditions, and radially confined by a harmonic potential of the form $1/2 m \omega_\perp^2 r^2$, with $r^2 = y^2 + z^2$, $\omega_\perp = 2\pi \times 150$ Hz, with $\sqrt{\hbar/m\omega_\perp} \ll L$. The gas is subjected to an external periodic potential along x of the form $V_{\text{ext}} = s E_R \cos(qx)$, where $E_R = \hbar^2 q^2 / 2m$ is the recoil energy, and the dimensionless parameter s gives the strength of the external potential. At zero temperature, the gas forms a Bose-Einstein condensate, characterized by a healing length $\xi = \hbar/(\sqrt{2m\mu_0})$, which represents the length scale on which the condensate can react to an external potential. We choose the period of the lattice $d = 2\pi/q = 4$ μm to be much larger than the healing length: $d \approx 16.7\xi$. In the opposite regime, $d \ll \xi$, the superfluid fraction becomes density independent and the kinematic Doppler shift is recovered [35]. An example of the transversely integrated GPE ground state density $\rho_{\text{GP}}(x)$ is reported in Fig. 1(a). A permanent current, providing a superfluid velocity $v_s^0 = 47.8$ μm/s, satisfying the proper boundary condition, is applied to the system. Following a previously proposed method for probing excitations [19,36], the system is prepared in a stationary state in the presence of a small additional potential $\lambda \cos(kx)$, which is suddenly removed. Since we are interested in the lowest energy modes, we take
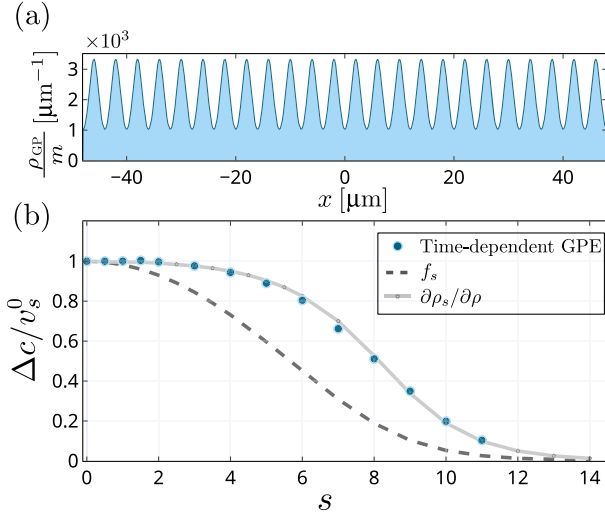
FIG. 1. (a) Example of a transversely integrated fluid density in an optical lattice of strength $s = 3$. (b) Doppler shift relative to v_s^0 of fourth sound in an optical lattice as a function of the strength parameter s. Numerical results of time-dependent GPE (points) are compared with the hydrodynamic prediction from Eq. (3) (solid line) and with the kinematic estimate $\Delta c / v_s^0 = f_s$ (dashed line).

the smallest possible value $k = 2\pi/L$, corresponding to a wavelength much larger than the transverse size of the gas. Within linear response theory, the time evolution of the average $\langle \cos(kx) \rangle$ contains the frequencies of the modes excited by the perturbation. In the absence of current, the signal contains a single frequency ω, from which the speed of sound is determined as $c = \omega/k$. The current induces a mode splitting ($\omega^+ \neq \omega^-$), from which the Doppler shift $2\Delta c = (\omega^+ - \omega^-)/k$ can be extracted.

In Fig. 1(b), we report the Doppler shift of fourth sound predicted by time-dependent GPE (dots), along with the HD prediction Eq. (3) (solid line), as well as with the kinematic estimate $\Delta c / v_s^0 = f_s$ (dashed line). The quantities entering the HD equations are coarse grained and correspond to averages over the distances characterizing the microscopic density modulations of the system. A typical example of a coarse-grained average is the Leggett upper bound for the superfluid density [37,38]: $L\rho_s^{-1} = \int dx / \rho_{GP}(x)$. It provides a very accurate estimate for ρ_s in the present configuration (see, e.g., [39]). The quantity $\partial \rho_s / \partial \rho$ entering Eq. (3) is obtained by determining the ground state of the system and extracting the superfluid density using Leggett's upper bound for different atom numbers. For the chosen parameters, we see that there exists a broad region in the lattice depth s where the kinematic shift substantially underestimates the Doppler effect.

Doppler effect in a supersolid—Supersolids are systems that present both superfluid and crystalline long-range order, which, consequently, show two classes of phononic (Nambu-Goldstone) modes [21], due to the simultaneous

and spontaneous breaking of U(1) symmetry and Galilean invariance hereafter called first (c_1) and second (c_2) sounds. With respect to the case of fourth sound, the HD theory of supersolid includes additional equations for the current (following from momentum conservation) and for $u_x := \partial_x u$, where u is the lattice displacement (following from crystalline long-range order) (see, e.g., [40–43] and Supplemental Material [44]),

$$\partial_t \rho + \partial_x j = 0, \tag{4}$$

$$\partial_t j + \partial_x \left(p + \rho_n v_n^2 + \rho_s v_s^2 \right) = 0, \tag{5}$$

$$\partial_t v_s + \partial_x (v_n v_s + \mu) = 0, \tag{6}$$

$$\partial_t u_x + \partial_x (v_n u_x - v_n) = 0, \tag{7}$$

where we remind the reader that ρ_n, v_n (ρ_s, v_s) are the normal (superfluid) density and velocity in the two-fluid model, $\rho = \rho_n + \rho_s$ is the total density, and $j = \rho_n v_n + \rho_s v_s$ is the total current. The quantities p and μ are the pressure and the chemical potential in the presence of stationary flow [45]. Since we are interested in the linear expansion of the HD equations, the constitutive relations can be written as [43,48]

$$\delta \mu = \frac{1}{\rho \kappa} \delta \rho + \gamma u_x + \frac{\rho_s'}{2} \delta w^2 - \frac{1}{2} \delta v_n^2, \tag{8}$$

$$\delta p = \left(\frac{1}{\kappa} - \gamma \right) \delta \rho + (\gamma \rho - \lambda) u_x + \frac{\rho_n - \rho \rho_n'}{2} \delta w^2, \tag{9}$$

$$\delta \rho_n = \rho_n' \delta \rho + \rho_n^u u_x, \tag{10}$$

where we introduce the relative velocity $w \equiv v_n - v_s$, γ as the strain-density constant, and λ as the elastic constant. For the sake of notation, we define $\rho_i' := \partial \rho_i / \partial \rho$, with $i = n, s$, and $\rho_n^u := \partial \rho_n / \partial u_x$. The dependence of ρ_n on the velocity difference w is quadratic and can be consequently neglected at the linear order. In order to calculate the speeds of sound, we linearize Eqs. (4)–(7) around their stationary values $\{n^0, v_s^0, v_n^0, u_x^0 = 0\}$ and determine the dispersion relation to the lowest order in the stationary velocities. We find four phononic modes $\omega_{1,2}^\pm = c_{1,2}^\pm |q|$, where the speeds of sound can be written as $c_{1,2}^\pm = c_{1,2}^0 \pm (v_s^0 + w^0 \delta_{1,2})$. The expressions for the two speeds of sound at rest $c_{1,2}^0$ in the supersolid phase have been already derived in a number of previous works [43,49–51] (see below). When $w^0 = 0$, i.e., the superfluid and normal components move together as a single fluid, both sounds are simply shifted by the kinematic Doppler effect, fixed by the fluid velocity $v_s^0 = v_n^0$. When $w^0 \neq 0$, we instead find the additional contribution $w^0 \delta_{1,2}$, with

$$\delta_{1,2} = \frac{\frac{\rho_n^u}{2\rho_n}\left[(c_{1,2}^0)^2 - c_\kappa^2 + \gamma\right] + 2(c_{1,2}^0)^2 - (1+f_s)c_\kappa^2 - \rho_n'\beta + \gamma\left[1 + \frac{\rho_n'}{\rho_n}(\rho - 2\rho_n)\right]}{2(c_{1,2}^0)^2 - c_\kappa^2 - \beta + 2\gamma}, \tag{11}$$

where $c_\kappa = \kappa^{-1/2}$ and $\beta = \lambda/\rho_n$, and the speeds of sound at rest are $(c_{1,2}^0)^2 = (A \pm \sqrt{A^2 - 4B})/2$ with $A = c_\kappa^2 + \beta - 2\gamma$ and $B = f_s(\beta c_\kappa - \gamma^2/f_n)$, where $f_n = 1 - f_s$ [44]. In the limit of an incompressible lattice, i.e., as $\beta \to \infty$, the Doppler shift approaches the value $\rho_s' v_s^0 + \rho_n' v_n^0$, which coincides with the result obtained above for fourth sound. Moreover, approaching the crystal phase, i.e., $\rho_n \to \rho$ ($\rho_n^u \to 0, \rho_n' \to 1$), one finds $\delta_{1,2} \to 1$, confirming the intuitive result that, in the crystal phase, the sound speed simply feels a kinematic Doppler shift, given by the normal velocity v_n^0.

In general, Eq. (11) predicts that the Doppler effect affects differently the two sound speeds. This result corresponds to the zero-temperature analog of the predictions obtained for the first and second sound velocities in superfluid ^{4}He [1,4].

We explore the HD prediction for the Doppler effect in the case of a Bose-Einstein condensed gas of atoms interacting with dipolar forces, where successful experimental achievements of supersolid configurations have been obtained in the last few years (see, e.g., [12] and references therein). Theoretically, the supersolid phase in such systems is stabilized by the inclusion of the so-called Lee-Huang-Yang correction to the mean-field approach, yielding an extended version of the GPE [52], which has been already employed to predict the sound velocities in the absence of persistent currents. Within such a formalism, the speeds of sound can be extracted following the protocol previously described for the fourth sound of a Bose-Einstein condensate in an optical lattice. In the absence of a persistent current, we already successfully applied the protocol to the supersolid phase of ultracold dipolar gases in [36].

In particular, we consider $N = 1.6 \times 10^5$ ^{164}Dy atoms confined, as before, in a tube of length $L = 96$ μm with periodic boundary conditions and with a transverse potential given by $m\omega_\perp^2 r^2/2$, where $\omega_\perp = 2\pi \times 100$ Hz. Dipoles are aligned by an external magnetic field along the z direction. The phase diagram of dipolar gases is characterized by the ratio ϵ_{dd} between the dipolar and contact two-body interaction strengths. Depending on its value, the system can be in a homogeneous superfluid, supersolid, or independent cluster phase, in which the superfluid long-range order along x is lost (see, e.g., [24–26,53]). Fixing the value of ϵ_{dd}, we prepare the initial state of the system by evolving the extended GPE in imaginary time in the moving frame with velocity V. We change the reference frame by adding the term $-VP_x$ to the extended GPE Hamiltonian, where P_x is the momentum operator along x.

One can prove that such an approach unequivocally determines both the superfluid and the normal velocities [44]. In particular, the velocity of the normal component coincides with the velocity of the moving frame ($v_n^0 = V$), while the appearance of the supercurrent is dictated by the energy minimization condition in the same moving frame. The quantized superfluid velocity exhibits the first jump to a finite value $v_s^0 = 2\pi\hbar/(mL)$ at the critical value $V^{cr} = v_n^{cr} = \hbar\pi/(mL) = 12.7$ μm/s (see also [54,55] for the current generation in a ring).

It is worth noticing that both v_n^0 and v_s^0 could be, in principle, fixed in an independent way, by properly modifying the phase pattern ϕ with imprinting techniques. The value of the superfluid velocity is determined by the phase winding at the boundaries of the configuration, while the velocity of the normal component is determined by the space variations of the phase at a microscopic scale, fixed, in the case of a supersolid, by the interdroplet distance (see Supplemental Material [44]). However, such a state would not, in general, correspond to an equilibrium configuration in the moving frame.

In Fig. 2(a), we report the transversely integrated density $\rho_{GP}(x)$ and the phase pattern $\phi(x,0,0)$ along the center of the tube for $v_n^0 = v_n^{cr}$ and $v_s^0 = 0$. As mentioned above, one can see that the phase of a supersolid shows spatial modulations, whose gradients are related to the velocity of the normal component [44]. In Fig. 2(b), we show the values of v_s^0, with its characteristic jump, as a function of the reference frame velocity V (for completeness also $v_n^0 = V$ is shown) [44].

The supersolid phase at rest exhibits two phononic modes, each of which splits into two in the presence of a current. As a consequence, as predicted by HD theory of supersolids (see discussion above), four different frequencies with linear dispersion $\omega = c|q| = c \times 2\pi/L$ are expected to occur. An example of Doppler splitting of the two sound modes $c_{1,2}$ in the supersolid phase is presented in Figs. 2(c) and 2(d). Both sounds experience an abrupt change of their speed at $V/v_n^{cr} = 1$, i.e., when the phase of the order parameter starts hosting a quantum of circulation. Let us also notice that, remarkably, the Doppler shift for the sound speed c_2 can be negative, i.e., the velocity c_2^+ of the phonon copropagating with the current is smaller than c_2^0 [shaded region in Fig. 2(d)]. Formally, the negative Doppler shift occurs for $v_n^0/v_s^0 < 1 - 1/\delta_2$ [44].

In order to make a quantitative comparison between the GPE and the predictions of the linearized hydrodynamic equations, we need to calculate the parameters entering the HD result (11). The parameters entering the speeds of
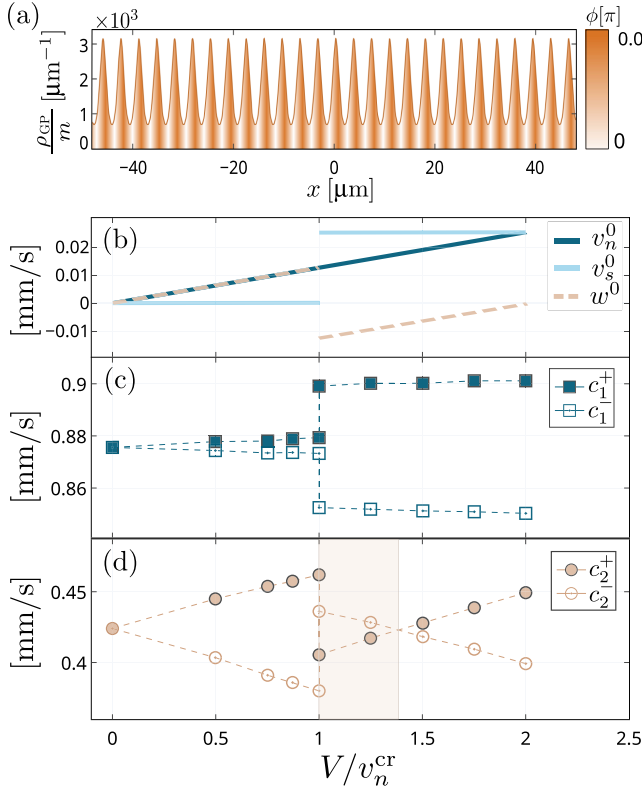
FIG. 2.   (a) Transversely integrated density of a supersolid at $\epsilon_{dd} = 1.398$ and its phase pattern at the tube's center (color scale) moving with $v_n^0 = v_n^{cr}$ and $v_s^0 = 0$. (b) Normal and superfluid velocities and their difference w^0 in a stationary state as a function of reference frame velocity V. Shapes of all three curves are independent of ϵ_{dd}. Bottom panels present splitting of the (c) first and (d) second sound into four phonon modes for the system presented in (a). Within the shaded area, the Doppler shift of the second sound becomes negative.
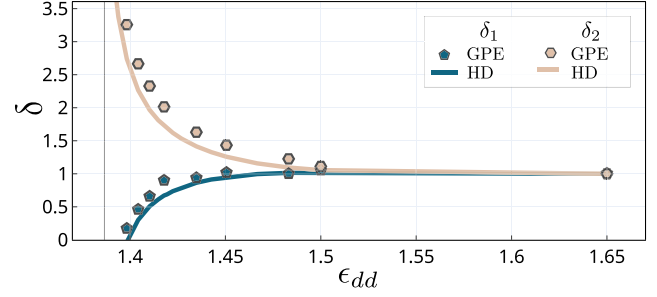

FIG. 3.   Anomalous Doppler shift of the first and second sound in the supersolid phase. Results of time-dependent simulations (markers) are compared with the hydrodynamic model (solid lines). The gray vertical line marks the superfluid-supersolid transition point.

sound in the absence of permanent currents (f_s, κ, β, and γ) have been discussed in previous works [36,51] (see also Supplemental Material [44]). In particular, the strain-density coupling γ has been shown to be very small for the supersolid phase of a dipolar gas [51] and will be neglected in our analysis. The new parameters ρ_n' and ρ_s' are determined numerically by marginally changing the total atom number N, while the derivative ρ_n^u, quantifying the change in the normal density with respect to $\partial_x u$, is calculated by varying the interdroplet distance [44].

To test the hydrodynamic predictions, we extract the anomalous Doppler term δ_i [see Eq. (11)] from the difference $\frac{1}{2}(c_i^+ - c_i^-)$ calculated in the time-dependent GPE simulation. In Fig. 3, we show the comparisons between the HD theory (lines) and the numerical results (symbols). The good agreement between the hydrodynamic and time-dependent GPE predictions confirms the highly nontrivial form of the Doppler effect in supersolids. The effect is especially pronounced close to the superfluid-supersolid phase transition.

Conclusions—We have provided analytic and numerical predictions for the zero-temperature Doppler effect exhibited by ultracold atomic gases in the presence of density modulations caused by external periodic potentials, as well as by the spontaneous breaking of translational symmetry (supersolids). Analytic results are derived by linearizing the hydrodynamic theory of superfluids and supersolids and compared with dynamic simulations based on the numerical solution of the GPE. We have shown that in single component superfluids anomalous Doppler shifts, following from the occurrence of a relative motion between the superfluid and normal velocities, can take place even at zero temperature, thanks to the breaking of Galilean invariance, causing the appearance of the normal component. In the presence of an optical lattice, only fourth sound can propagate, and the Doppler effect takes a particularly simple form fixed by the density derivative of the superfluid density. For supersolids, where there exist sounds of hybrid superfluid and crystalline nature, Doppler shifts exhibit highly nontrivial features, and for certain values of the parameters the shift can even have a negative sign. We have considered the case of very elongated configurations that could be experimentally implemented, confining the atomic gas in a ring geometry and where one-dimensional hydrodynamic theory can be safely applied.

[1] I. Khalatnikov, The propagation of sound in moving helium II and the effect of a thermal current upon the propagation of second sound, Zh. Eksp. Teor. Fiz. **30**, 617 (1956) [Sov. Phys. JETP **3**, 649 (1956)], http://jetp.ras.ru/cgi-bin/e/index/e/3/4/p649?a=list.

[2] I. Rudnick, H. Kojima, W. Veith, and R. S. Kagiwada, Observation of superfluid-helium persistent current by Doppler-shifted splitting of fourth-sound resonance, Phys. Rev. Lett. **23**, 1220 (1969).

[3] D. J. Bergman, B. I. Halperin, and P. C. Hohenberg, Hydrodynamic theory applied to fourth sound in a moving superfluid, Phys. Rev. B **11**, 4253 (1975).

[4] Y. A. Nepomnyashchy, Unusual Doppler effect in He II, Phys. Rev. B **47**, 905 (1993).

[5] Y. Nepomnyashchy and M. Revzen, Curious Doppler shift of fourth sound in the low temperature limit, Phys. Lett. A **161**, 164 (1991).

[6] N. Gov, A. Mann, Y. Nepomnyashchy, and M. Revzen, Unusual Doppler shift of fourth sound in a ^{3}He-^{4}He mixture, Phys. Lett. A **182**, 149 (1993).

[7] A. M. Kenis, Y. A. Nepomnyashchy, A. Mann, and M. Revzen, Unusual Doppler effect in the B phase of superfluid ^{3}He, Phys. Rev. Lett. **82**, 584 (1999).

[8] D. F. Società Italiana, *Bose-Einstein Condensation in Atomic Gases* (IOS Press, Amsterdam, NY, 1999).

[9] I. Bloch, J. Dalibard, and W. Zwerger, Many-body physics with ultracold gases, Rev. Mod. Phys. **80**, 885 (2008).

[10] L. Pitaevskii and S. Stringari, *Bose-Einstein Condensation and Superfluidity* (Oxford University Press, Oxford, 2016).

[11] M. Lewenstein, A. Sanpera, and V. Ahufinger, *Ultracold Atoms in Optical Lattices* (Oxford University Press, London, England, 2016).

[12] A. Recati and S. Stringari, Supersolidity in ultracold dipolar gases, Nat. Rev. Phys. **5**, 735 (2023).

[13] C. Fort, F. S. Cataliotti, L. Fallani, F. Ferlaino, P. Maddaloni, and M. Inguscio, Collective excitations of a trapped Bose-Einstein condensate in the presence of a 1d optical lattice, Phys. Rev. Lett. **90**, 140405 (2003).

[14] G. Chauveau, C. Maury, F. Rabec, C. Heintze, G. Brochier, S. Nascimbene, J. Dalibard, J. Beugnon, S. M. Roccuzzo, and S. Stringari, Superfluid fraction in an interacting spatially modulated Bose-Einstein condensate, Phys. Rev. Lett. **130**, 226003 (2023).

[15] J. Tao, M. Zhao, and I. B. Spielman, Observation of anisotropic superfluid density in an artificial crystal, Phys. Rev. Lett. **131**, 163401 (2023).

[16] L. Tanzi, S. M. Roccuzzo, E. Lucioni, F. Famà, A. Fioretti, C. Gabbanini, G. Modugno, A. Recati, and S. Stringari, Supersolid symmetry breaking from compressional oscillations in a dipolar quantum gas, Nature (London) **574**, 382 (2019).

[17] G. Natale, R. M. W. van Bijnen, A. Patscheider, D. Petter, M. J. Mark, L. Chomaz, and F. Ferlaino, Excitation spectrum of a trapped dipolar supersolid and its experimental evidence, Phys. Rev. Lett. **123**, 050402 (2019).

[18] M. Guo, F. Böttcher, J. Hertkorn, J.-N. Schmidt, M. Wenzel, H. P. Büchler, T. Langen, and T. Pfau, The low-energy Goldstone mode in a trapped dipolar supersolid, Nature (London) **574**, 386 (2019).

[19] A. Kumar, N. Anderson, W. D. Phillips, S. Eckel, G. K. Campbell, and S. Stringari, Minimally destructive, Doppler measurement of a quantized flow in a ring-shaped Bose–Einstein condensate, New J. Phys. **18**, 025001 (2016).

[20] A. F. Andreev and I. M. Lifshitz, Quantum theory of defects in crystals, Sov. Phys. JETP **29**, 1107 (1969), http://jetp.ras.ru/cgi-bin/e/index/e/29/6/p1107?a=list.

[21] H. Watanabe and T. c. v. Brauner, Spontaneous breaking of continuous translational invariance, Phys. Rev. D **85**, 085010 (2012).

[22] J. Léonard, A. Morales, P. Zupancic, T. Esslinger, and T. Donner, Supersolid formation in a quantum gas breaking a continuous translational symmetry, Nature (London) **543**, 87 (2017).

[23] J.-R. Li, J. Lee, W. Huang, S. Burchesky, B. Shteynas, F. Top, A. O. Jamison, and W. Ketterle, A stripe phase with supersolid properties in spin–orbit-coupled Bose–Einstein condensates, Nature (London) **543**, 91 (2017).

[24] L. Tanzi, E. Lucioni, F. Famà, J. Catani, A. Fioretti, C. Gabbanini, R. N. Bisset, L. Santos, and G. Modugno, Observation of a dipolar quantum gas with metastable supersolid properties, Phys. Rev. Lett. **122**, 130405 (2019).

[25] L. Chomaz, D. Petter, P. Ilzhöfer, G. Natale, A. Trautmann, C. Politi, G. Durastante, R. M. W. van Bijnen, A. Patscheider, M. Sohmen, M. J. Mark, and F. Ferlaino, Long-lived and transient supersolid behaviors in dipolar quantum gases, Phys. Rev. X **9**, 021012 (2019).

[26] F. Böttcher, J.-N. Schmidt, M. Wenzel, J. Hertkorn, M. Guo, T. Langen, and T. Pfau, Transient supersolid properties in an array of dipolar quantum droplets, Phys. Rev. X **9**, 011051 (2019).

[27] J. R. Pellam, Wave transmission and reflection phenomena in liquid helium II, Phys. Rev. **73**, 608 (1948).

[28] K. R. Atkins, Third and fourth sound in liquid helium II, Phys. Rev. **113**, 962 (1959).

[29] H. Kojima, W. Veith, S. J. Putterman, E. Guyon, and I. Rudnick, Vortex-free Landau state in rotating superfluid helium, Phys. Rev. Lett. **27**, 714 (1971).

[30] V. L. Pokrovskii and I. M. Khalatnikov, Hamiltonian formalism in classical and two-fluid hydrodynamics, Pis'ma Zh. Eksp. Teor. Fiz. **23**, 653 (1976), http://jetpletters.ru/ps/1806/article_27603.shtml.

[31] While for Bose superfluids the mass m coincides with the atomic mass, for a Fermi superfluid m is twice the atomic mass.

[32] An experimental verification of the hydrodynamic relation between c_0 and f_s was obtained only recently in [14,15].

[33] A. Smerzi and A. Trombettoni, Nonlinear tight-binding approximation for Bose-Einstein condensates in a lattice, Phys. Rev. A **68**, 023613 (2003).

[34] E. Taylor and E. Zaremba, Bogoliubov sound speed in periodically modulated Bose-Einstein condensates, Phys. Rev. A **68**, 053611 (2003).

[35] A. Smerzi, A. Trombettoni, P. G. Kevrekidis, and A. R. Bishop, Dynamical superfluid-insulator transition in a chain of weakly coupled Bose-Einstein condensates, Phys. Rev. Lett. **89,** 170402 (2002).

[36] M. Šindik, T. Zawiślak, A. Recati, and S. Stringari, Sound, superfluidity, and layer compressibility in a ring dipolar supersolid, Phys. Rev. Lett. **132,** 146001 (2024).

[37] A. J. Leggett, Can a solid be "superfluid"?, Phys. Rev. Lett. **25,** 1543 (1970).

[38] A. J. Leggett, On the superfluid fraction of an arbitrary many-body system at $T = 0$, J. Stat. Phys. **93,** 927 (1998).

[39] J. C. Smith, D. Baillie, and P. B. Blakie, Supersolidity and crystallization of a dipolar Bose gas in an infinite tube, Phys. Rev. A **107,** 033301 (2023).

[40] D. T. Son, Effective Lagrangian and topological interactions in supersolids, Phys. Rev. Lett. **94,** 175301 (2005).

[41] M. Liu, Two possible types of superfluidity in crystals, Phys. Rev. B **18,** 1165 (1978).

[42] W. M. Saslow, Microscopic and hydrodynamic theory of superfluidity in periodic solids, Phys. Rev. B **15,** 173 (1977).

[43] C.-D. Yoo and A. T. Dorsey, Hydrodynamic theory of supersolids: Variational principle, effective Lagrangian, and density-density correlation function, Phys. Rev. B **81,** 134518 (2010).

[44] See Supplemental Material at http://link.aps.org/supplemental/10.1103/PhysRevLett.134.226001 for more details.

[45] Here we wrote the chemical potential μ in the laboratory frame. Using $\mu_s - \mu = v_n v_s - \frac{1}{2} v_s^2$ [46,47] one can recover the standard form of Eq. (6) (see also [44]).

[46] S. J. Putterman, *Superfluid Hydrodynamics*, North-Holland series in low temperature physics Vol. 3 (North-Holland, Amsterdam, 1974).

[47] I. M. Khalatnikov, *An Introduction to the Theory of Superfluidity*, Advanced book classics (Addison-Wesley, Redwood City, CA, 1988).

[48] M. Liu, Superfluid dynamics, equilibrium conditions, and centripetal forces, J. Stat. Mech. (2023) 033104.

[49] Y. Pomeau and S. Rica, Dynamics of a model of supersolid, Phys. Rev. Lett. **72,** 2426 (1994).

[50] J. Hofmann and W. Zwerger, Hydrodynamics of a superfluid smectic, J. Stat. Mech. (2021) 033104.

[51] L. M. Platt, D. Baillie, and P. B. Blakie, Sound waves and fluctuations in one-dimensional supersolids, Phys. Rev. A **110,** 023320 (2024).

[52] F. Wächtler and L. Santos, Quantum filaments in dipolar Bose-Einstein condensates, Phys. Rev. A **93,** 061603(R) (2016).

[53] S. M. Roccuzzo and F. Ancilotto, Supersolid behavior of a dipolar Bose-Einstein condensate confined in a tube, Phys. Rev. A **99,** 041601(R) (2019).

[54] M. N. Tengstrand, D. Boholm, R. Sachdeva, J. Bengtsson, and S. M. Reimann, Persistent currents in toroidal dipolar supersolids, Phys. Rev. A **103,** 013313 (2021).

[55] M. Nilsson Tengstrand, P. Stürmer, J. Ribbing, and S. M. Reimann, Toroidal dipolar supersolid with a rotating weak link, Phys. Rev. A **107,** 063316 (2023).

Sound, Superfluidity, and Layer Compressibility in a Ring Dipolar Supersolid

Marija Šindik©,* Tomasz Zawiślak©,* Alessio Recati©,† and Sandro Stringari©

Pitaevskii BEC Center, CNR-INO and Dipartimento di Fisica, Università di Trento, Via Sommarive 14, 38123 Povo, Trento, Italy

We propose a protocol to excite the Goldstone modes of a supersolid dipolar Bose-Einstein condensed gas confined in a ring geometry. By abruptly removing an applied periodic modulation proportional to $\cos(\varphi)$, where φ is the azimuthal angle, we explore the resulting oscillations of the gas by solving the extended Gross-Pitaevskii equation. The value of the two longitudinal sound velocities exhibited in the supersolid phase are analyzed using the hydrodynamic theory of supersolids at zero temperature, which explicitly takes into account both the superfluid and the crystal nature of the system. This approach allows for the determination of the layer compressibility modulus as well as of the superfluid fraction, f_S, in agreement with the Leggett estimate of the nonclassical moment of inertia.

A key consequence of the spontaneous breaking of continuous symmetries is the occurrence of Goldstone modes, which, in the presence of finite range interactions, take the form of gapless excitations in the long wavelength limit. The identification and the experimental observation of the Goldstone modes, then, represents a question of central interest in various fields of science, including elementary particle physics, magnetism, superfluidity, and superconductivity. The recent realization of supersolidity has raised the question of the identification of the corresponding Goldstone modes, which are the consequence of the spontaneous and simultaneous breaking of phase symmetry and translational invariance, ensuring the nonintuitive coexistence of superfluid and crystal features. From the theoretical side, the study of the Goldstone modes in supersolids has a long history, starting from the pioneering work of Andreev and Lifshitz [1] (see also [2–6]), and more recent papers based on numerical simulations on atomic Bose gases interacting with soft-core potentials [7–9], spin orbit coupled gases (see the recent reviews [10,11] and reference therein), condensation in multimode cavity [12], and dipolar gases [13] (see also the recent perspective [14] and references therein). First experimental evidence for the occurrence of dispersive Goldstone modes in a supersolid has been recently reported in the case of a dipolar gas confined in a harmonic trap, where the modes take the form of discretized oscillations and in particular with the emergence of novel crystal-like oscillations as soon as one enters the supersolid phase [15–17].

The use of harmonic trapping potentials, inducing the nonhomogeneity of the gas, together with the appearance of a number of droplets that form the nonsuperfluid (crystal) component of the gas, limits, however, the possibility to fully appreciate the rich dynamics of the dipolar gas as a bulk supersolid. Theoretically, the speeds of sounds for soft-core [7,8] and dipolar [13,18] gases in the thermodynamic limit have already been the object of numerical simulations in the supersolid phase, based on the use of proper periodic boundary conditions. In particular, in the very recent work [18], which appeared while completing our work, a detailed analysis of the two longitudinal sounds along an infinite tube has been reported as a function of the relevant interaction parameters. Experimentally, reaching the thermodynamic limit in a dipolar gas is, however, strongly inhibited if one uses box potentials because of the tendency of the dipoles to accumulate near the borders of the wall, giving rise to typical edge effects [19,20].

For the above reasons, in this Letter we propose to use a ring potential, which naturally fulfills the periodic boundary conditions along the azimuthal angle direction, allowing for an efficient way to approach the thermodynamic limit. Ring traps provide a simple realization of matter wave circuits, with important perspectives in the emerging field of atomtronics [21,22]. The longitudinal Goldstone modes of the ring trapped dipolar gas are then excited by suddenly removing a periodic annular perturbation and the resulting values of the sound velocities are analyzed using the hydrodynamic theory of supersolids. Supersolid hydrodynamics actually provides fundamental new insights on the origin of the two sound modes. In particular, employing the calculated values of the sound velocities, we determine for the first time the layer compressibility modulus and confirm the prediction for the superfluid fraction of a dipolar gas in the supersolid phase based on the nonclassical moment of inertia and its concurrence with Leggett's estimation [23].

The model and its quantum phases.—In a dilute dipolar Bose gas, the atoms interact by a delta-contact potential $V_c(\mathbf{r}) = g\delta(\mathbf{r})$, with the coupling constant $g = 4\pi\hbar^2 a/m > 0$ fixed by the atomic mass m and the s-wave scattering length

a; and by the dipolar potential $V_{dd}(\mathbf{r}) = (\mu_0 \mu^2/4\pi)[(1 - 3\cos^2\theta)/|\mathbf{r}|^3]$ with θ the angle between $\mathbf{r}$ and the direction z of the externally applied magnetic field, which aligns the atomic magnetic dipole moments μ. The most important parameter to determine the zero temperature phase diagram of the gas is the ratio between the strengths of the contact and the dipolar interactions, $\epsilon_{dd} = a_{dd}/a$ with $a_{dd} = \mu_0 \mu^2/12\pi\hbar^2$, the so-called dipolar length. For small enough ϵ_{dd} the system forms a Bose-Einstein condensate (BEC) (superfluid phase), while by increasing it beyond a certain threshold, in three-dimensional uniform configurations, the system collapses due to the attractive nature of the dipolar interaction. Confining the gas along the z direction prevents this collapse, and three distinct phases occur: (i) a homogeneous BEC (superfluid phase), (ii) a supersolid phase in a very small interval of ϵ_{dd}, and (iii) a droplet crystal phase, i.e., independent droplets arranged in a crystal structure. In the present Letter we consider moreover that the gas is confined in the x-y plane by a ring-shaped potential $V_{ext}(r_\perp, z) = m[\omega_\perp^2(r_\perp - R_0)^2 + \omega_z^2 z^2]/2$ with $r_\perp = \sqrt{x^2 + y^2}$, of radius $R_0 = 7.64$ μm and trap frequencies $\omega_z = \omega_\perp = 2\pi \times 100$ Hz, leading to the three phases reported in Fig. 2, calculated for $N = 80\,000$ ^{164}Dy atoms, corresponding to $a_{dd} = 132a_0$, where a_0 is the Bohr radius. We obtain a ring-shaped cloud of length $L \approx 49$ μm [24] and width FWHM$_{XY}$ changing from 1.41 μm in the superfluid to 0.7 μm approaching the crystal phase (see Fig. 2). Because of magnetostriction, the cloud is elongated in the third direction with FWHM$_Z \approx 4$ μm. The system is numerically studied within the so-called extended Gross-Pitaevskii equation [25], which in the last few years has been systematically employed to describe the equilibrium and dynamic properties of dipolar supersolids in reasonably good agreement with the experimental findings.

The protocol.—We first determine the state of the gas by applying a small static perturbation of the form $-V_0 \cos\varphi$, where φ is the azimuthal angle along the ring, which produces stationary density modulations. We then suddenly set $V_0 = 0$, resulting in the excitation of the longitudinal phonon modes propagating along the ring. Similar protocols have been already applied to investigate the Doppler effect due to the presence of quantized vortices in a ring [26] and, more recently, to investigate the effect of superfluidity on the propagation of sound in a dilute Bose gas confined in a box in the presence of an external periodic potential [27].

An easy analysis of the response of the system can be obtained considering sufficiently large ring sizes for which the ring can be mapped in a linear tube configuration with imposed periodic boundary conditions. In particular, we assume that the length L of the ring is much larger than its width, so that one can safely identify $\cos(\varphi)$ with $\cos(qx)$, where $q = 2\pi/L$ is the wave vector of the longitudinal excitation and the variable x, with $0 \le x \le L$, is the longitudinal coordinate along the tube. According to linear response theory, the quantity $F(t) = \langle\cos\varphi\rangle(t)$ should show, in the supersolid phase, a beating of two modes (see inset in Fig. 3),

$$F(t) = V_0 \sum_{i=\pm} \chi_i(q) \cos(\omega_i(q)t), \quad (1)$$

with $\omega_i(q)$ approaching, for sufficiently small q (and hence large L), the linear phonon dispersion $\omega_i(q) \simeq c_i q$, with c_+ and c_- hereafter called upper and lower sound velocities, respectively. The quantities $\chi_i(q)$, $i = \pm$, define the contributions of the two modes to the static response and hence to the compressibility sum rule according to

$$\chi(q) = \chi_+(q) + \chi_-(q) = \int_0^\infty d\omega \frac{S(q,\omega)}{\omega} \underset{q\to 0}{=} \frac{N\kappa}{2}, \quad (2)$$

with κ the compressibility of the system (hereafter, we set $\hbar = m = 1$, with m the atomic mass), while $S(q,\omega)$ is the dynamic structure factor. From the analysis of the measurable signal $F(t)$ of Eq. (1) one can then determine the sound velocities c_+ and c_-, and the relative contribution

$$R \equiv \frac{\chi_-}{\chi} = \frac{c_+^2 - c_\kappa^2}{c_+^2 - c_-^2} \quad (3)$$

of the lowest (lower sound) mode to the compressibility sum rule, where we have defined $c_\kappa = \sqrt{\kappa^{-1}}$. Analogously, the contribution of lower sound to the f sum rule $m_1 = \int_0^\infty d\omega S(q,\omega)\omega = Nq^2/2$ is given by

$$\frac{m_1^{(-)}}{m_1} = \frac{c_-^2}{c_\kappa^2} \frac{c_+^2 - c_\kappa^2}{c_+^2 - c_-^2}. \quad (4)$$

However, in the vicinity of the superfluid-supersolid phase transition, within the supersolid region, we find that our perturbation excites additional modes and Eqs. (3) and (4), based on the two-mode approximation, are less accurate.

Hydrodynamic model for supersolidity.—Since the two sound modes are the Nambu-Goldstone bosons due to the spontaneous breaking of translational symmetry and the $U(1)$ symmetry related to the conserved particle number, the low-energy dynamics of a supersolid exhibits universal features and can be described by hydrodynamics [1–4,28]. In the following we will use the hydrodynamic approach to supersolidity recently elaborated by Hofmann and Zwerger [6], inspired by the work of Yoo and Dorsey [5]. This formulation, applicable to Galilean invariant systems, is particularly suitable to investigate the behavior of longitudinal phonons in the presence of a layer structure. This is reasonably well realized in highly elongated configurations of a dipolar supersolid, where the droplets effectively play the role of the layers. Neglecting the effects of the strain density coupling included in the general formulation of

supersolid hydrodynamics [5,29], the approach, in this minimal hydrodynamic formulation, provides the following expression for the two sound velocities [6]:

$$c_\pm^2 = \frac{c_\kappa^2}{2}\left[1 + \beta\kappa \pm \sqrt{(1+\beta\kappa)^2 - 4f_S\beta\kappa}\right], \quad (5)$$

which depends on three fundamental parameters: the velocity c_κ, fixed by the compressibility parameter κ; the renormalized layer compressibility modulus $\beta = B/\rho_n$, given by the layer compressibility modulus B [30] divided by the normal density $\rho_n = \bar{\rho} - \rho_s$; and the superfluid fraction $f_S = \rho_s/\bar{\rho}$, with $\bar{\rho}$ the average 1D density. In our one-dimensional structure, B is the only elastic constant, corresponding to the energy cost due to the change in the separation between the peaks. The relevant parameters $\beta\kappa$ and f_S can be expressed in terms of the upper and lower sound velocities according to the relations $\beta\kappa = (c_+^2 + c_-^2)/c_\kappa^2 - 1$ and $f_S\beta\kappa = c_+^2 c_-^2/c_\kappa^4$, which directly follow from Eq. (5).

Let us now discuss the consequences of the hydrodynamic model in different phases of dipolar Bose gases.

(i) Superfluid phase ($f_S = 1$ and $\beta = 0$): Only the upper solution (upper sound) of Eq. (5) is relevant and $c_+ = c_\kappa$.

(ii) Supersolid phase ($0 < f_s < 1$ and $\beta \neq 0$): In this most interesting case the deviations of the sound speeds from c_κ are determined by the dimensionless combination $\beta\kappa$ and by the superfluid fraction f_S. In particular, near the transition to the crystal phase, where the superfluid fraction is expected to vanish, the sound velocities approach the values

$$c_+ \to \sqrt{1 + \beta\kappa - \frac{f_S\beta\kappa}{1+\beta\kappa}}c_\kappa, \quad c_- \to \sqrt{f_S\frac{\beta\kappa}{1+\beta\kappa}}c_\kappa, \quad (6)$$

while the ratio R given by Eq. (3) approaches the value $\beta\kappa/(1 + \beta\kappa)$. It is worth noticing the close analogy between Eq. (6) and the dependence of the second sound velocity on the superfluid density predicted by Landau's two-fluid hydrodynamic theory at finite temperature [31] (see also [32]).

It is also interesting to note that when the combination $\beta\kappa$ becomes very large the lower sound velocity takes the form $c_- = \sqrt{f_S}c_\kappa$ in the whole supersolid phase, it exhausts the compressibility sum rule, while its relative contribution to the f-sum rule [see Eq. (4)] exactly coincides with the superfluid fraction f_S. These results are consistent with the behavior of a superfluid in the presence of an optical lattice, where translational invariance is not broken spontaneously and the upper mode $\omega_+ = c_+q$ is replaced by a gapped excitation.

(iii) Crystal phase ($f_s = 0$ and $\beta \neq 0$): Only the upper solution survives in this case and the sound velocity takes

the simple expression $c_+ = c_\kappa\sqrt{1+\beta\kappa}$. Notice however that, differently from what happens in the superfluid phase, the upper sound mode, while exhausting the f-sum rule, does not exhaust the compressibility sum rule, revealing the occurrence of a diffusive mode at zero frequency. Such a mode represents the natural continuation of the lower sound mode beyond the transition to the crystal phase [33] and corresponds to the diffusive permeation mode of a smectic-A liquid crystal [6,33]. The evolution of the lower mode from a propagating to a diffusive one, is analogous to the fate of second sound in a uniform fluid above the superfluid critical temperature (see, e.g., [34,35]).

Results.—The compressibility κ of the gas can be extracted from the knowledge of the density changes caused by the static perturbation $-V_0\cos(\varphi)$ according to linear response theory [see Eq. (2)]. Another option, which would not require the actual knowledge of V_0, is to measure the relative contribution R [see Eq. (3)] of the lower sound mode to the compressibility sum rule through the weights of the beating signal of Eq. (1).

Our protocol actually measures the static response function $\chi(q)/N$ [see Eqs. (1) and (2)], which coincides with the compressibility κ only in the long-wavelength limit $q \to 0$. Because of the finite size of the ring, the lowest accessible value is $q = 2\pi/L$, and it is consequently important to control the difference between $\chi(q = 2\pi/L)/N$ and the compressibility parameter $\kappa = (\bar{\rho}\partial\mu/\partial\bar{\rho})^{-1}$, where μ is the chemical potential. In our case the difference turns out to be about 15% in the superfluid phase and up to 30% close to the crystal phase. For consistency, we have used the values of κ given by the "measured" values $\chi(q = 2\pi/L)$. On the other hand, we verified that the superfluid fraction f_S, obtained by applying the hydrodynamic model to the results of the extended Gross-Pitaevskii simulation employing our protocol, is much less sensitive to finite size effects.

To illustrate the potential of the proposed protocol, in Fig. 1 we report the dispersion for larger values of q, within the superfluid phase, obtained by applying a perturbation
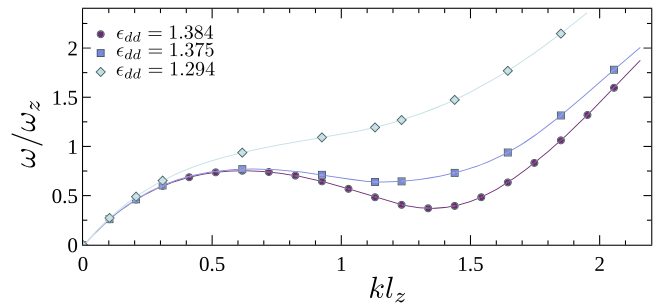

FIG. 1. Dispersion relation obtained using the proposed protocol for three values of ϵ_{dd} approaching the superfluid-supersolid phase transition. The roton minimum softens near $k = \sqrt{2}/l_z$, where $l_z = \sqrt{\hbar/m\omega_z}$ is the harmonic oscillator length along the confined direction [37].
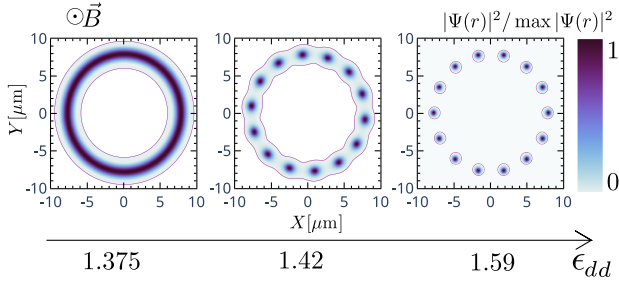
FIG. 2. Density plots of $N = 80\,000$ ^{164}Dy atoms in the superfluid, supersolid and crystal phase (left, middle, and right panel, respectively), integrated over the z axis, along which the magnetic field $\vec{B}$ is aligned. Red contours mark 1% of the relative density $|\Psi(\mathbf{r})|^2 / \max |\Psi(\mathbf{r})|^2$.

proportional to $\cos(n\varphi)$ with $n = 1, 2, \ldots$, giving access to the phonon-maxon-roton dispersion, for which experimental evidence was reported in a superfluid dipolar gas using Bragg spectroscopy [36]. The figure clearly shows that the roton minimum becomes more pronounced as one approaches the transition to the supersolid phase, which in our configuration occurs for $\epsilon_{dd} = 1.387$.

In Fig. 2 we show the density profiles in the ring geometry calculated in the superfluid, supersolid, and crystal phases [38]. In our simulations, based on the extended Gross-Pitaevskii equation, we have considered configurations with the same number of droplets (equal to 14) in both the supersolid and crystal phases. Actually, exact energy minimization would predict a decrease of the number of droplets when one approaches the transition to the crystal phase, leading to the small discontinuities in the resulting values of the observed quantities, which do not however affect the main conclusions of our work. The pinning of the number (and position) of droplets can be achieved by introducing a small additional periodic potential during the initial stage of the supersolid state preparation. During the time evolution, once the periodic potential is removed, we observe that the number of droplets remains constant.

Figures 3 and 4 report the main results of our work, based on the combined application of the protocol and of the hydrodynamic model of supersolids. In Fig. 3 we show the calculated upper and lower sound velocities as a function of ϵ_{dd}, together with the value of c_κ, which coincides with the sound velocity in the superfluid phase. The figure clearly reveals the decrease of the lower sound velocity as one approaches the transition to the crystal phase. Similar features have been reported in [18] obtained for an infinite tube, confirming that our mesoscopic system correctly approaches the thermodynamic limit. We include also the lowest order expressions for the two sound speeds when $f_s \to 0$, Eq. (6) (red and green continuous lines), which are seen to be in good agreement with the calculated values also when the superfluid density is not that small.
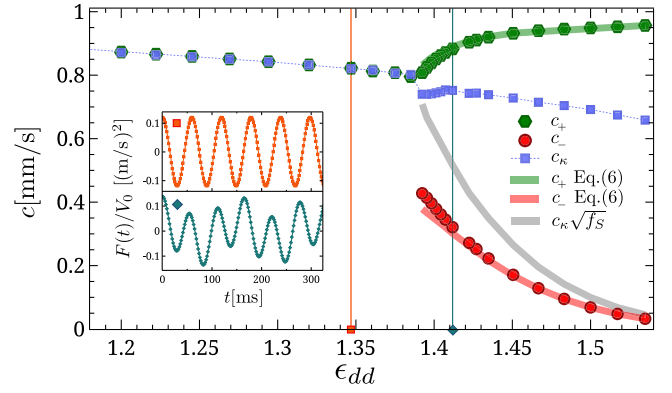

FIG. 3. Sound velocities c_+ and c_- determined with the protocol (green hexagons and red circles respectively) across the superfluid-supersolid phase transition. The blue squares correspond to $c_\kappa(q = 2\pi/L)$. Both sound speeds are well captured by Eq. (6) (green and red solid lines) even far from the crystal phase. For completeness we also report the values $\sqrt{f_S}c_\kappa$ (gray solid line) found for an incompressible lattice (see text). The inset presents the time evolution of F for two values of ϵ_{dd} marked with solid lines of corresponding colors. The data points are fitted with one (two) cosines in the superfluid (supersolid) phase with excellent quality.
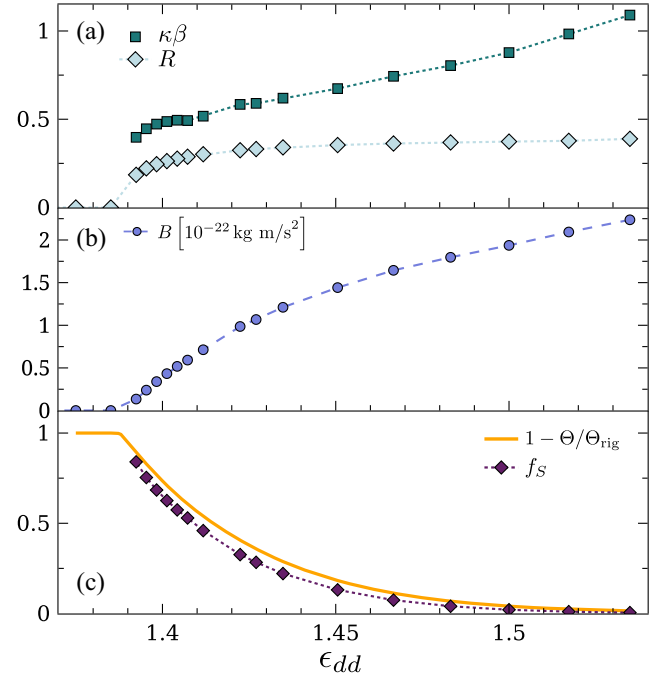

FIG. 4. Panel (a) displays dimensionless parameters $\kappa\beta$ calculated using the hydrodynamic model (green squares), and the ratio $R = \chi_-/\chi$ (light blue diamonds) extracted from the time evolution of Eq. (1). In panel (b) we show the emergence of finite layer compressibility modulus B. In panel (c) we compare the extracted value of superfluid fraction f_S (purple diamonds) using the hydrodynamic relations Eq. (5), with the value determined via the nonclassical fraction of moment of inertia Eq. (7) (orange line).

For comparison we also show the prediction $c_- = \sqrt{f_S} c_\kappa$ (gray continuous line), which would hold in the presence of an optical lattice ($B \to \infty$) and which badly reproduces the actual values of c_- in the supersolid phase. The standard hydrodynamic expression $c = \sqrt{f_S} c_\kappa$ was actually successfully employed by Tao *et al.* [40] and Chauvaeau *et al.* [27] to extract the value of f_S of a BEC gas in the presence of an optical lattice (not a supersolid).

In Fig. 4(a) we report the results for the relevant parameter $\beta\kappa$ of the hydrodynamic model and the ratio R. An interesting outcome of our analysis is that while the speeds of sound, the compressibility, and the dimensionless parameter $\beta\kappa$ show a jump at the superfluid-supersolid transition, the contribution of lower sound to the compressibility sum rule, R, goes smoothly to zero. The same continuous vanishing is observed for the layer compressibility modulus B, as shown in Fig. 4(b). In Fig. 4(c) we report the value of the superfluid fraction f_S, predicted by the analysis of the sound velocities: $f_S = c_+^2 c_-^2 / c_\kappa^2 (c_+^2 + c_-^2 - c_\kappa^2)$. As already pointed out above, we have verified that this value of f_S is very weakly sensitive to finite size effects. Furthermore, repeating the simulations with a larger value of the phonon wave vector, $q = 4\pi/L$, rather than $2\pi/L$, we find that f_S is modified only by a few percent. Since the oscillation frequency has also almost doubled, this would allow working on shorter timescales, thereby reducing the consequences of the finite lifetime of the system.

Moment of inertia and superfluid fraction.—Both the layer compressibility and the superfluid fraction can, in principle, be calculated from Gross-Pitaevskii theory (see, for example, Josserand *et al.* [29]). In fact, the superfluid fraction has been the object of several calculations based on extended Gross-Pitaevskii theory (see, e.g., [13,18,41]) for dipolar gases showing one-dimensional periodic configurations. In our narrow ring configuration, the superfluid fraction essentially coincides with the nonclassical fraction of the moment of inertia

$$f_S \simeq 1 - \frac{\Theta}{\Theta_{\text{rig}}}, \qquad (7)$$

which is reported in Fig. 4(c) (orange line) for the comparison with the value extracted from the calculated sound velocities. The moment of inertia Θ is fixed by the value $\langle J_z \rangle$ of the angular momentum induced by a rotational constraint of the form $-\Omega J_z$, according to the relation $\Theta = \lim_{\Omega \to 0} \langle J_z \rangle / \Omega$, while $\Theta_{\text{rig}} = N\langle x^2 + y^2 \rangle$ is the classical rigid value [42]. We also verified that f_S from Eq. (7) practically coincides with the rigorous Leggett's upper bound $2\pi [\bar{\rho} \int_0^{2\pi} d\varphi / \rho(\varphi)]^{-1} \geq f_S$, where $\rho(\varphi)$ is the transverse integrated density along the ring [43].

The good agreement between the two predictions shown in Fig. 4(c) reveals the consistency of the extended Gross-Pitaevskii theory with the hydrodynamic model of supersolidity.

In conclusion, we have suggested (i) a protocol to determine the Goldstone modes of a supersolid dipolar gas confined in a ring and (ii) a way to identify the relevant parameters of the hydrodynamic theory of supersolids.

Our work, in particular, paves the way for an experimental determination of the layer compressibility modulus and of the superfluid fraction, based on the measurement of sound velocities. On the theory side, our findings can be used to extract the supersolid hydrodynamic parameters in the thermodynamic limit by using the available estimations of the sound speeds in infinite systems [13,18].

Finally, it is worth noticing that our protocol for the extraction of the speed of sound and of the hydrodynamic parameters is not limited to the dipolar supersolid platform we discuss in this Letter. It can be equally applied to dipolar mixtures, which are expected to show longer lifetimes than single-component dipolar gases [44–47], and whose spectrum has been very recently addressed in [48]. Another very interesting system for the application of our protocol are semiconductor dipolar excitons, where ring configurations naturally occur (see, e.g., [49,50] and references therein), and cluster crystallization has been observed [51,52].

*These authors contributed equally to this work.
†Corresponding author: alessio.recati@ino.cnr.it

[1] A. F. Andreev and I. M. Lifshitz, Quantum theory of defects in crystals, Sov. Phys. JETP **29**, 1107 (1969), http://www.jetp.ras.ru/cgi-bin/dn/e_029_06_1107.pdf.

[2] W. M. Saslow, Microscopic and hydrodynamic theory of superfluidity in periodic solids, Phys. Rev. B **15**, 173 (1977).

[3] D. T. Son, Effective Lagrangian and topological interactions in supersolids, Phys. Rev. Lett. **94**, 175301 (2005).

[4] C. Josserand, Y. Pomeau, and S. Rica, Coexistence of ordinary elasticity and superfluidity in a model of a defect-free supersolid, Phys. Rev. Lett. **98**, 195301 (2007).

[5] C.-D. Yoo and A. T. Dorsey, Hydrodynamic theory of supersolids: Variational principle, effective Lagrangian, and density-density correlation function, Phys. Rev. B **81**, 134518 (2010).

[6] J. Hofmann and W. Zwerger, Hydrodynamics of a superfluid smectic, J. Stat. Mech. (2021) 033104.

[7] S. Saccani, S. Moroni, and M. Boninsegni, Excitation spectrum of a supersolid, Phys. Rev. Lett. **108,** 175301 (2012).

[8] T. Macrì, F. Maucher, F. Cinti, and T. Pohl, Elementary excitations of ultracold soft-core bosons across the superfluid-supersolid phase transition, Phys. Rev. A **87,** 061602(R) (2013).

[9] F. Ancilotto, M. Rossi, and F. Toigo, Supersolid structure and excitation spectrum of soft-core bosons in three dimensions, Phys. Rev. A **88,** 033618 (2013).

[10] A. Recati and S. Stringari, Coherently coupled mixtures of ultracold atomic gases, Annu. Rev. Condens. Matter Phys. **13,** 407 (2022).

[11] G. I. Martone, Bose-Einstein condensates with Raman-induced spin-orbit coupling: An overview, Europhys. Lett. **143,** 25001 (2023).

[12] N. Masalaeva, H. Ritsch, and F. Mivehvar, Tuning photon-mediated interactions in a multimode cavity: From supersolid to insulating droplets hosting phononic excitations, Phys. Rev. Lett. **131,** 173401 (2023).

[13] S. M. Roccuzzo and F. Ancilotto, Supersolid behavior of a dipolar Bose-Einstein condensate confined in a tube, Phys. Rev. A **99,** 041601(R) (2019).

[14] A. Recati and S. Stringari, Supersolidity in ultracold dipolar gases, Nat. Rev. Phys. **5,** 735 (2023).

[15] L. Tanzi, S. M. Roccuzzo, E. Lucioni, F. Famà, A. Fioretti, C. Gabbanini, G. Modugno, A. Recati, and S. Stringari, Supersolid symmetry breaking from compressional oscillations in a dipolar quantum gas, Nature **574,** 382 (2019).

[16] M. Guo, F. Böttcher, J. Hertkorn, J.-N. Schmidt, M. Wenzel, H. P. Büchler, T. Langen, and T. Pfau, The low-energy Goldstone mode in a trapped dipolar supersolid, Nature (London) **574,** 386 (2019).

[17] G. Natale, R. M. W. van Bijnen, A. Patscheider, D. Petter, M. J. Mark, L. Chomaz, and F. Ferlaino, Excitation spectrum of a trapped dipolar supersolid and its experimental evidence, Phys. Rev. Lett. **123,** 050402 (2019).

[18] P. B. Blakie, L. Chomaz, D. Baillie, and F. Ferlaino, Compressibility and speeds of sound across the superfluid-to-supersolid phase transition of an elongated dipolar gas, Phys. Rev. Res. **5,** 033161 (2023).

[19] H.-Y. Lu, H. Lu, J.-N. Zhang, R.-Z. Qiu, H. Pu, and S. Yi, Spatial density oscillations in trapped dipolar condensates, Phys. Rev. A **82,** 023622 (2010).

[20] S. M. Roccuzzo, S. Stringari, and A. Recati, Supersolid edge and bulk phases of a dipolar quantum gas in a box, Phys. Rev. Res. **4,** 013086 (2022).

[21] L. Amico *et al.*, Roadmap on atomtronics: State of the art and perspective, AVS Quantum Sci. **3,** 039201 (2021).

[22] L. Amico, D. Anderson, M. Boshier, J.-P. Brantut, L.-C. Kwek, A. Minguzzi, and W. von Klitzing, Colloquium: Atomtronic circuits: From many-body physics to quantum technologies, Rev. Mod. Phys. **94,** 041001 (2022).

[23] A. J. Leggett, On the superfluid fraction of an arbitrary many-body system at $T = 0$, J. Stat. Phys. **93,** 927 (1998).

[24] The cloud's shape is influenced by long-ranged dipolar repulsion effectively increasing its radius.

[25] F. Wächtler and L. Santos, Quantum filaments in dipolar Bose-Einstein condensates, Phys. Rev. A **93,** 061603(R) (2016).

[26] A. Kumar, N. Anderson, W. D. Phillips, S. Eckel, G. K. Campbell, and S. Stringari, Minimally destructive, Doppler measurement of a quantized flow in a ring-shaped Bose–Einstein condensate, New J. Phys. **18,** 025001 (2016).

[27] G. Chauveau, C. Maury, F. Rabec, C. Heintze, G. Brochier, S. Nascimbene, J. Dalibard, J. Beugnon, S. M. Roccuzzo, and S. Stringari, Superfluid fraction in an interacting spatially modulated Bose-Einstein condensate, Phys. Rev. Lett. **130,** 226003 (2023).

[28] Y. Pomeau and S. Rica, Dynamics of a model of supersolid, Phys. Rev. Lett. **72,** 2426 (1994).

[29] C. Josserand, Y. Pomeau, and S. Rica, Patterns and supersolids, Eur. Phys. J. Special Topics **146,** 47 (2007).

[30] P. M. Chaikin and T. C. Lubensky, *Principles of Condensed Matter Physics* (Cambridge University Press, Cambridge, England, 1995).

[31] L. Landau, Theory of the superfluidity of helium II, Phys. Rev. **60,** 356 (1941).

[32] L. Pitaevskii and S. Stringari, *Bose-Einstein Condensation and Superfluidity* (Oxford University Press, New York, 2016).

[33] P. C. Martin, O. Parodi, and P. S. Pershan, Unified hydrodynamic theory for crystals, liquid crystals, and normal fluids, Phys. Rev. A **6,** 2401 (1972).

[34] W. F. Vinen, *Physics of Quantum Fluids*, edited by R. Kubo and F. Takano (Syokabo Publishing Company, Tokyo, 1970).

[35] H. Hu, E. Taylor, X.-J. Liu, S. Stringari, and A. Griffin, Second sound and the density response function in uniform superfluid atomic gases, New J. Phys. **12,** 043040 (2010).

[36] D. Petter, G. Natale, R. M. W. van Bijnen, A. Patscheider, M. J. Mark, L. Chomaz, and F. Ferlaino, Probing the roton excitation spectrum of a stable dipolar Bose gas, Phys. Rev. Lett. **122,** 183401 (2019).

[37] L. Santos, G. V. Shlyapnikov, and M. Lewenstein, Roton-maxon spectrum and stability of trapped dipolar Bose-Einstein condensates, Phys. Rev. Lett. **90,** 250403 (2003).

[38] Ring configurations of similar shape, hosting a supersolid dipolar gas with persistent currents, were considered in [39].

[39] M. N. Tengstrand, D. Boholm, R. Sachdeva, J. Bengtsson, and S. M. Reimann, Persistent currents in toroidal dipolar supersolids, Phys. Rev. A **103,** 013313 (2021).

[40] J. Tao, M. Zhao, and I. B. Spielman, Observation of anisotropic superfluid density in an artificial crystal, Phys. Rev. Lett. **131,** 163401 (2023).

[41] J. C. Smith, D. Baillie, and P. B. Blakie, Supersolidity and crystallization of a dipolar Bose gas in an infinite tube, Phys. Rev. A **107,** 033301 (2023).

[42] The energy dependence on angular momentum for such rotating configurations at larger Ω has recently been explored in [39].

[43] The good agreement between Leggett's upper bound and the superfluid fraction calculated in an infinite tube by means of effective mass was recently discussed in [41].

[44] H. Saito, Y. Kawaguchi, and M. Ueda, Ferrofluidity in a two-component dipolar Bose-Einstein condensate, Phys. Rev. Lett. **102**, 230403 (2009).

[45] T. Bland, E. Poli, L. A. Pena Ardila, L. Santos, F. Ferlaino, and R. N. Bisset, Alternating-domain supersolids in binary dipolar condensates, Phys. Rev. A **106**, 053322 (2022).

[46] S. Li, U. N. Le, and H. Saito, Long-lifetime supersolid in a two-component dipolar Bose-Einstein condensate, Phys. Rev. A **105**, L061302 (2022).

[47] D. Scheiermann, L. A. Pena Ardila, T. Bland, R. N. Bisset, and L. Santos, Catalyzation of supersolidity in binary dipolar condensates, Phys. Rev. A **107**, L021302 (2023).

[48] W. Kirkby, A.-C. Lee, D. Baillie, T. Bland, F. Ferlaino, P. B. Blakie, and R. N. Bisset, Excitations of a binary supersolid, arXiv:2312.03390.

[49] R. Rapaport and G. Chen, Experimental methods and analysis of cold and dense dipolar exciton fluids, J. Phys. Condens. Matter **19**, 295207 (2007).

[50] M. Combescot, R. Combescot, and F. Dubin, Bose–Einstein condensation and indirect excitons: A review, Rep. Prog. Phys. **80**, 066501 (2017).

[51] L. V. Butov, A. C. Gossard, and D. S. Chemla, Macroscopically ordered state in an exciton system, Nature (London) **418**, 751 (2002).

[52] S. V. Andreev, Fragmented-condensate solid of dipolar excitons, Phys. Rev. B **95**, 184519 (2017).

Letter

Creation and robustness of quantized vortices in a dipolar supersolid when crossing the superfluid-to-supersolid transition

Marija Šindik [1,2] Alessio Recati,[1,3,*] Santo Maria Roccuzzo,[4] Luis Santos,[5,†] and Sandro Stringari[1,3]

[1]*Pitaevskii BEC Center, CNR-INO and Dipartimento di Fisica, Università di Trento, 38123 Trento, Italy*
[2]*Institute of Physics Belgrade, University of Belgrade, 11080 Belgrade, Serbia*
[3]*Trento Institute for Fundamental Physics and Applications, INFN, 38123 Trento, Italy*
[4]*Kirchhoff-Institut fur Physik, Ruprecht-Karls-Universitat Heidelberg, 69120 Heidelberg, Germany*
[5]*Institut für Theoretische Physik, Leibniz Universität Hannover, 30167 Hannover, Germany*

We study quantized vortices in dipolar supersolids at the transition between the superfluid and the supersolid phase. We present an approach to the nucleation of vortices and their observation, based on the quenching of the *s*-wave scattering length across the phase transition. Starting from a slowly rotating, vortex-free configuration in the superfluid phase, we predict vortex nucleation as the system enters the supersolid phase, due to the strong reduction of the critical angular velocity in the supersolid. Once a vortex is created, we show that it is robustly preserved when the condensate is brought back to the superfluid phase, where it may be readily observed. These results may have a significant impact on ongoing experiments, given that the observation of quantized vortices would constitute a key probe of the superfluid character of dipolar supersolids.

Quantized vortices constitute a key hallmark of superfluidity [1]. They are topological defects of the order parameter, and therefore robust with respect to perturbations in the U(1) broken symmetry phase. Ultracold gases are an ideal platform for the study of vortices. In these gases, vortices are typically created either by stirring the cloud with a laser, or by rotating a slightly deformed trap. Vortices are detected, after a condensate expansion, by the observation of the density holes corresponding to the vortex cores. Vortices have been observed both in Bose-Einstein condensates (BECs) [2–4] and in superfluid spin-1/2 Fermi gases [5]. The angular momentum and its quantization in the presence of a vortex can be inferred by exploiting the lift in the degeneracy of quadrupole-mode frequencies due to broken time-reversal symmetry [6], as observed in condensates [7,8].

Supersolids constitute a particularly intriguing phase in which superfluidity coexists with a modulated density [9]. In the last few years, supersolidity has attracted major attention in ultracold gases. Experiments on BECs in optical cavities have revealed supersolidlike properties [10]. Condensates with an imposed one-dimensional spin-orbit coupling have been shown to present a supersolid stripe phase [11,12]. Recent experiments on BECs of magnetic atoms have revealed the creation of supersolids of ultradilute droplets maintained by the interplay between attractive mean-field interactions and the effective repulsion induced by quantum fluctuations [13]. Dipolar supersolids have attracted quickly growing interest, and successful experiments in droplet arrays have studied the phase coherence [14–17], the appearance of Goldstone

modes in the excitation spectrum [18–20], and the peculiar dynamics related to scissors modes [21–24]. Very recently, two-dimensional supersolid configurations have been also realized [25,26].

Recent theoretical works have investigated quantum vortices in dipolar supersolids [27,28]. Quantum vortices in a supersolid were first discussed in Ref. [29] in the context of a hypothetical supersolid phase of helium. There it was shown, in the context of a mean-field Gross-Pitaevskii formalism employing a repulsive soft-core interaction, that vortices may be nucleated in the supersolid by an obstacle. It was suggested as well that vortices could be robust when crossing back and forth the superfluid-to-supersolid transition. A peculiar feature pointed out in Ref. [27] in the case of supersolid dipolar gases is that vortices are, both energetically and dynamically, more favored in the supersolid phase than in the superfluid one. The low-density regions surrounding the droplets of the supersolid phase help in reducing the energetic barrier for a vortex to enter the system, and in pinning the vortices in the interstitials between droplets [27]. Even a very slow rotation of the trapping potential can then trigger the dynamical instability that drives vortex nucleation [27]. However, the direct detection of vortices formed in the interstitials is largely inhibited because, even in the absence of vortices, this region is characterized by a very low density.

In this Letter, we first explore in detail the robustness of vortices in dipolar BECs when crossing the superfluid-to-supersolid transition, showing that the conservation of angular momentum results in a peculiar dynamic behavior, since the value of the angular momentum per particle associated to a vortex is markedly different in the superfluid and in the supersolid phase. Using the difference in the vortex properties in both phases, we propose a dynamic protocol based on the

---

*Corresponding author: alessio.recati@ino.it
†Corresponding author: santos@itp.uni-hannover.de

quench of a slowly rotating dipolar condensate from the superfluid into the supersolid phase. A vortex is nucleated in the supersolid due to the strongly reduced critical angular velocity, and a subsequent quench back allows for straightforward vortex imaging in the superfluid phase. Our protocol could provide not only the experimental proof of vortex nucleation in a dipolar supersolid, but also allows for directly probing the modified vortex properties in that phase [27], as, e.g., the reduction of the critical angular velocity for vortex nucleation. It has the advantage of avoiding the nucleation of vortices starting from the equilibrium configuration in the supersolid phase, whose implementation is notoriously more difficult due to three-body collisions.

Model. We consider a BEC of atoms with mass m and magnetic dipole moment μ aligned along the z axis, trapped in a harmonic potential of the form $V_{ext}(\mathbf{r}) = m\omega_\perp^2[(1 - \varepsilon)x^2 + (1 + \varepsilon)y^2 + \lambda^2 z^2]/2$.

At zero temperature the physics of the system is well described by the extended Gross-Pitaevskii equation (eGPE) [30,31],

$$i\hbar\frac{\partial\Psi(\mathbf{r},t)}{\partial t} = \left[-\frac{\hbar^2\nabla^2}{2m} + V_{ext}(\mathbf{r}) + g|\Psi(\mathbf{r},t)|^2 \right.$$
$$\left. + \int d\mathbf{r}'V_{dd}(\mathbf{r} - \mathbf{r}')|\Psi(\mathbf{r}',t)|^2 + \gamma|\Psi(\mathbf{r},t)|^3\right]$$
$$\times \Psi(\mathbf{r},t), \qquad (1)$$

where $g = 4\pi\hbar^2 a/m > 0$ is the coupling constant fixed by the s-wave scattering length a, and $V_{dd}(\mathbf{r}) = \frac{\mu_0\mu^2}{4\pi}\frac{1-3\cos^2\theta}{|\mathbf{r}|^3}$ is the dipole-dipole interaction, with θ the angle between $\mathbf{r}$ and the z axis. The last term in Eq. (1) is given by the repulsive Lee-Huang-Yang (LHY) correction induced by quantum fluctuations, with

$$\gamma = \frac{32ga^{3/2}}{3\sqrt{\pi}}\text{Re}\left[\int_0^1 du[1 + \epsilon_{dd}(3u^2 - 1)]^{5/2}\right], \qquad (2)$$

where $\epsilon_{dd} = \mu_0\mu^2/3g$ characterizes the relative strength of the dipolar interaction with respect to the contact one. The eGPE has been systematically employed in the last few years to investigate quantum droplets and supersolidity in dipolar BECs [13].

For small-enough ϵ_{dd}, the system behaves as a standard condensate (superfluid phase). By decreasing the scattering length, and hence increasing the value of ϵ_{dd}, the role of the attractive part of the dipolar force becomes more important, and the LHY term starts playing a crucial role in determining the equilibrium solution. The LHY term ensures the stability of the system against collapse and eventually favors the formation of a periodic structure, which can be regarded as a series of dense droplets connected by a dilute superfluid gas (supersolid phase) [14–16]. A further increase of ϵ_{dd} leads to a state where the droplets are independent and mutually incoherent, and the system does not show any extended superfluidity (independent droplet phase).[1]

The supersolid phase can host quantized vortices [27]. As already anticipated in the Introduction, vortex nucleation is significantly favored by the reduced density in the interdroplet regions, but vortices nestle in those interstitials, making their experimental observation much more problematic than in the superfluid phase. Below, we first discuss the robustness of vortices when quenching the system across the superfluid-to-supersolid transition. We then exploit such a robustness to design a protocol that first allows for an alternative mechanism for the nucleation of vortices in the supersolid phase and, second, for probing their existence by imaging them in the superfluid phase, where they are more easily detectable, also owing to the large increase of their core size as compared to condensates with only contact interactions. This second step resembles the procedure used in the pioneering work of Ref. [5], where the vortices created in a strongly interacting Fermi gas were imaged by quenching from the BCS to the BEC regime, where their visibility was better ensured after gas expansion. In the case of dipolar gases the procedure is more challenging because the two regimes, supersolid and superfluid, are separated by a first-order phase transition and not connected by a continuous crossover.

Crossing the superfluid-to-supersolid transition. We consider a BEC of 4×10^4 ^{164}Dy atoms, confined in an axially symmetric trap ($\varepsilon = 0$) with $\omega_\perp = 2\pi \times 60$ Hz and $\lambda = 2$. Under these conditions, the superfluid-to-supersolid transition occurs at the value $a_{crit} = 94.6a_0$ (a_0 is the Bohr radius) corresponding to $\epsilon_{dd} = 1.395$.

Ground states of the system are calculated using imaginary-time evolution in the rotating frame, obtained by adding the constraint $-\Omega L_z$ to the eGPE (1), where Ω is the angular velocity, and L_z the z component of the angular momentum operator.[2] Above some critical angular velocity Ω_c, vortical solutions become energetically favorable. It is important to notice that Ω_c is significantly smaller than the one required for the dynamical vortex nucleation [27], associated with a quadrupolar instability, as we discuss later.

We first consider a vortex in the superfluid phase, obtained for $a = 105a_0 > a_{crit}$, and $\Omega = 0.22\omega_\perp > \Omega_c$ [see Fig. 1(a)(i)]. In the superfluid phase the vortex is characterized by an angular momentum $\hbar$ per particle. Starting from this ground-state configuration,[3] we ramp down in 100 ms the s-wave scattering length to a value $a = 94a_0 < a_{crit}$, which would correspond at equilibrium to the supersolid phase. Indeed, once the transition is crossed, a strong density modulation emerges on a very short timescale, leading to the formation of droplets. After a certain waiting time the system acquires a configuration close to the ground-state shape with a vortex in the supersolid phase [Fig. 1(a)(iii)]. It is, however, interesting to notice that in most cases we find a transient regime [see Fig. 1(a)(ii)] where the number of peaks is larger (four droplets) than in the final, ground-state-like configuration (three droplets). Despite the occurrence of small

---

[1]Notice, however, that each droplet is still superfluid.

[2]The critical value a_{crit} increases slightly by increasing Ω. Such a change is, however, less than 0.5% for the angular velocities used in this text.

[3]All the time-dependent simulations presented in this Letter are performed in the laboratory reference frame.
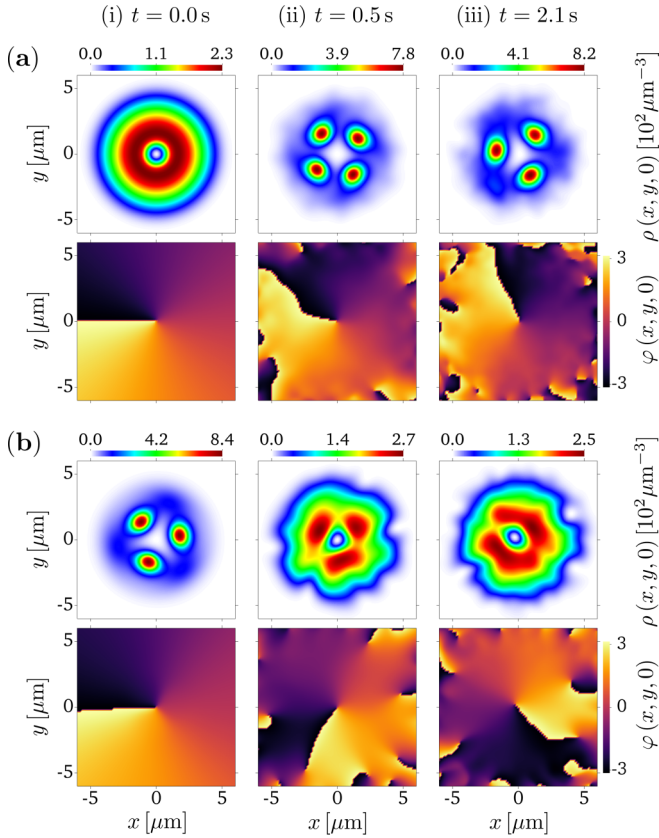
FIG. 1. Density and phase profiles in the $z = 0$ plane. (a) Vortex through the superfluid-to-supersolid crossing at $t = 0$, 0.5, and 2.1 s. The vortex is initially created in the superfluid regime ($\Omega/\omega_\perp = 0.22$, $a = 105a_0$), and a is then linearly ramped in 100 ms down to $94a_0$, within the supersolid phase. (b) Vortex through the supersolid-to-superfluid crossing for the same times. At $t = 0$, the vortex is in the supersolid phase ($\Omega/\omega_\perp = 0.16$, $a = 94a_0$). Then a is ramped in 100 ms up to $105a_0$, within the superfluid regime. In all cases, $\omega_\perp = 2\pi \times 60$ Hz, $\lambda = 2$, and $\varepsilon = 0$.

oscillations caused by the crossing of the first-order transition, the vortex survives at the trap center, with its characteristic phase pattern. Since angular momentum is conserved during the ramping of the scattering length, and since in the supersolid the angular momentum per particle carried by the vortex is smaller than $\hbar$ due to the reduced global superfluidity [27], the remaining angular momentum is carried by the droplets, whose centers of mass rotate in the laboratory frame with an angular velocity larger than Ω.

Crossing the supersolid-to-superfluid transition. We carry out the same analysis in the opposite direction, following the fate of a quantized vortex initially present in the supersolid phase, an especially relevant case for the protocol discussed below. As discussed in Ref. [27], the angular velocity Ω_c, for which the vortex becomes energetically favorable, is much smaller than the one in the superfluid phase. In Fig. 1(b)(i), we consider a configuration with $a = 94a_0$ and $\Omega = 0.16\omega_\perp$, slightly higher than the critical value Ω_c. The created vortex is characterized by an angular momentum per particle of $0.87\hbar$. After ramping in 100 ms the scattering length up to $a = 105a_0$ to reach the superfluid phase, we find that the vortex remains

clearly visible [Figs. 1(b)(ii) and 1(b)(iii)]. Note, however, that the density profile preserves some density modulations, which are the residue of the original droplets characterizing the supersolid phase. Moreover, since the overall angular momentum must be preserved, the larger angular momentum associated with the vortex in the superfluid phase ($\hbar$) is compensated by the rotational motion of the density modulations, and by the occurrence of antivortices located near the border of the atomic cloud, as well as, in some cases, by a slight displacement of the vortex core from the center of the trap.

Protocol for vortex nucleation and detection. We are now ready to discuss our protocol which combines the favorable nucleation mechanism of quantized vortices exhibited by the supersolid phase with their topological robustness when the supersolid-to-superfluid phase transition is crossed. Our starting point is a slowly rotating trapped dipolar gas in the superfluid phase ($a = 105a_0$), obtained by a sudden introduction of rotation to the superfluid ground state in a slightly deformed trap in the xy plane, and letting it equilibrate for 200 ms [see Fig. 2(a)]. In the laboratory frame this corresponds to choosing a harmonic potential of the form

$$V_{\text{ext}}(t) = \frac{m}{2}\omega_\perp^2\{(1-\varepsilon)[x\cos(\Omega t) + y\sin(\Omega t)]^2$$
$$+ (1+\varepsilon)[-x\sin(\Omega t) + y\cos(\Omega t)]^2 + \lambda^2 z^2\}. \quad (3)$$

We choose a slightly deformed trap ($\varepsilon = 6.6\%$) and an angular velocity ($\Omega = 0.3\omega_\perp$) such that the system is unable to nucleate vortices in the superfluid phase, as the quadrupole dynamical instability occurs at $0.45\omega_\perp$.[4] The parameters are instead large enough for vortex nucleation once the system enters the supersolid phase. Therefore we reduce the value of the scattering length with a linear ramp in 100 ms down to $a = 94a_0$. After entering the supersolid phase, first droplets are formed [Fig. 2(b)] and, after a while, a vortex is nucleated in the center [Fig. 2(c)]. Notice that the timescale for this process is slow in the present simulation. We expect, however, that in a real experimental situation the timescale will be much faster, as a consequence of thermal noise, which is not accounted for in our calculations. When the vortex is formed [Fig. 2(c)] we restore the isotropy of the trap ($\varepsilon = 0$) in order to ensure the robustness of the topological configuration associated with the vortex and the conservation of angular momentum. We ramp the scattering length back to its initial value (following a similar ramp) and after a while [Fig. 2(d)] the system enters again the superfluid phase. We then recover a very similar configuration as that of Fig. 1(b)(iii).

The same protocol may be employed for the nucleation of more than one vortex when increasing the angular velocity Ω of the rotating trap. In Fig. 3, we show our results for different angular velocities in our protocol. The upper panel shows the atomic cloud in the supersolid phase right before inverting the ramping of the scattering length. The lower panel depicts the final density distribution after ramping back the scattering length. The case with $\Omega = 0$ is important, since it clearly shows that despite the strong density modulation in the supersolid regime, once moving back into the superfluid no

_____

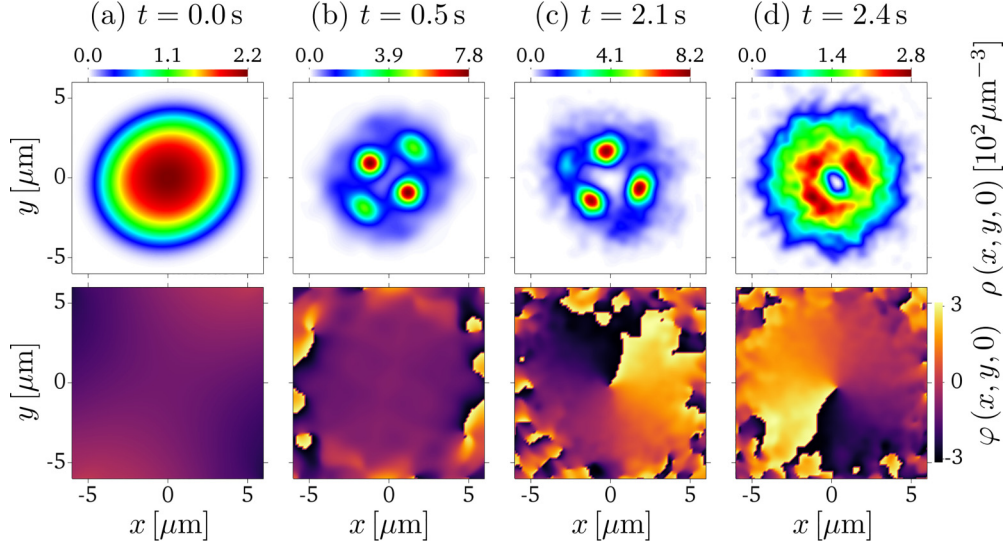[4]This value remains almost constant in the whole superfluid region.

FIG. 2. Density and phase profiles in the $z = 0$ plane, showing vortex nucleation employing the protocol discussed in the text. (a) Initial vortex-free superfluid with a scattering length $a = 105a_0$, confined in a slightly deformed harmonic trap ($\omega_\perp = 2\pi \times 60$ Hz, $\lambda = 2$, $\varepsilon = 6.6\%$), rotating with an angular velocity $\Omega = 0.3\omega_\perp$. (b) The scattering length is linearly ramped in 100 ms down to $a_s = 94a_0$, resulting in a transition to the supersolid phase. (c) After some time a vortex is nucleated at the center of the trap. (d) The isotropy of the trap is restored ($\varepsilon = 0$) and the scattering length is linearly ramped in 100 ms up to the initial value, resulting in a superfluid with a readily detectable vortex core.

core appears, the final density remains smooth and characterized by a maximum in the center, very similar to the initial equilibrium configuration. By increasing Ω we eventually observe one vortex nucleated in the center using $\Omega = 0.3\omega_\perp$ [same as Figs. 2(c) and 2(d)], two vortices using $\Omega = 0.35\omega_\perp$, and three vortices using $\Omega = 0.4\omega_\perp$. Note that in all cases the vortices are nucleated in the supersolid phase, since the

angular velocity is not large enough to create vortices in the superfluid.

Conclusions. We have studied vortices in a dipolar condensate when crossing the superfluid-to-supersolid transition. We have proposed in particular a protocol that should permit under realistic conditions to nucleate and detect quantized vortices in a dipolar supersolid, a major hallmark of
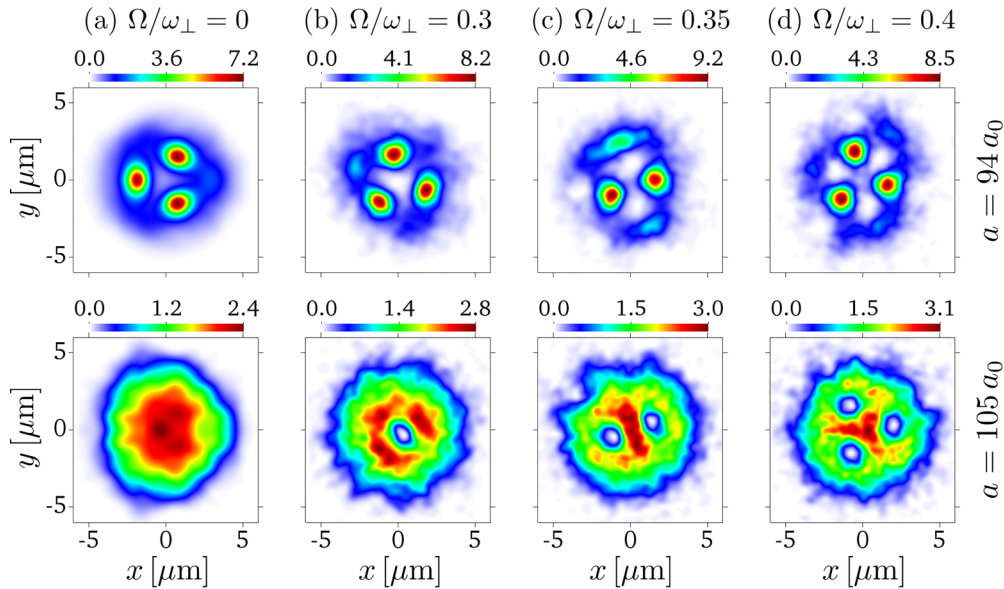

FIG. 3. Density profiles in the $z = 0$ plane. Results for the dynamical protocol for different angular velocities: $\Omega/\omega_\perp = 0$ (a), 0.3 (b), 0.35 (c), and 0.4 (d). The parameters and procedure are the same as in Fig. 2. The upper row corresponds to the configurations in the supersolid phase at $t = 2.1$ s, before inverting the ramp of the scattering length. The lower row corresponds to the final configuration in the superfluid phase (at $t = 2.4$ s) after ramping back the scattering length. Note that imaging in the superfluid phase should easily reveal the presence of no vortex, one, two, and three vortices, respectively. The final angular momentum per particle (once the isotropy of the xy trapping is restored) is (a) $L = 0$, (b) $L = 1.03\hbar$, (c) $L = 1.85\hbar$, and (d) $L = 2.42\hbar$.

superfluidity. The method is based on a controlled ramp of the scattering length across the superfluid-to-supersolid transition, employing the very nature of the supersolid to induce vortex nucleation. Although vortex detection is difficult in the supersolid since vortices gather in regions of very low density, a ramp back into the superfluid permits an easy imaging of the vortex core, even more so than in contact-interacting condensates due to the significantly larger vortex size in a dipolar BEC. Very recently, quantized vortices have been actually observed in the superfluid phase of a dipolar gas [32,33].

[1] L. Pitaevskii and S. Stringari, *Bose-Einstein Condensation and Superfluidity* (Oxford University Press, Oxford, UK, 2016).

[2] M. R. Matthews, B. P. Anderson, P. C. Haljan, D. S. Hall, C. E. Wieman, and E. A. Cornell, Phys. Rev. Lett. **83**, 2498 (1999).

[3] K. W. Madison, F. Chevy, W. Wohlleben, and J. Dalibard, Phys. Rev. Lett. **84**, 806 (2000).

[4] J. R. Abo-Shaeer, C. Raman, J. M. Vogels, and W. Ketterle, Science **292**, 476 (2001).

[5] M. W. Zwierlein, J. R. Abo-Shaeer, A. Schirotzek, C. H. Schunck, and W. Ketterle, Nature (London) **435**, 1047 (2005).

[6] F. Zambelli and S. Stringari, Phys. Rev. Lett. **81**, 1754 (1998).

[7] F. Chevy, K. W. Madison, and J. Dalibard, Phys. Rev. Lett. **85**, 2223 (2000).

[8] P. C. Haljan, I. Coddington, P. Engels, and E. A. Cornell, Phys. Rev. Lett. **87**, 210403 (2001).

[9] M. Boninsegni and N. V. Prokof'ev, Rev. Mod. Phys. **84**, 759 (2012).

[10] J. Léonard, A. Morales, P. Zupancic, T. Esslinger, and T. Donner, Nature (London) **543**, 87 (2017).

[11] J.-R. Li, J. Lee, W. Huang, S. Burchesky, B. Shteynas, F. Ç. Top, A. O. Jamison, and W. Ketterle, Nature (London) **543**, 91 (2017).

[12] K. T. Geier, G. I. Martone, P. Hauke, and S. Stringari, Phys. Rev. Lett. **127**, 115301 (2021).

[13] F. Böttcher, J.-N. Schmidt, J. Hertkorn, K. S. H. Ng, S. D. Graham, M. Guo, T. Langen, and T. Pfau, Rep. Prog. Phys. **84**, 012403 (2020).

[14] L. Tanzi, E. Lucioni, F. Famà, J. Catani, A. Fioretti, C. Gabbanini, R. N. Bisset, L. Santos, and G. Modugno, Phys. Rev. Lett. **122**, 130405 (2019).

[15] F. Böttcher, J.-N. Schmidt, M. Wenzel, J. Hertkorn, M. Guo, T. Langen, and T. Pfau, Phys. Rev. X **9**, 011051 (2019).

[16] L. Chomaz, D. Petter, P. Ilzhöfer, G. Natale, A. Trautmann, C. Politi, G. Durastante, R. M. W. van Bijnen, A. Patscheider, M. Sohmen *et al.*, Phys. Rev. X **9**, 021012 (2019).

[17] P. Ilzhöfer, M. Sohmen, G. Durastante, C. Politi, A. Trautmann, G. Natale, G. Morpurgo, T. Giamarchi, L. Chomaz, M. J. Mark *et al.*, Nat. Phys. **17**, 356 (2021).

[18] L. Tanzi, S. M. Roccuzzo, E. Lucioni, F. Famà, A. Fioretti, C. Gabbanini, G. Modugno, A. Recati, and S. Stringari, Nature (London) **574**, 382 (2019).

[19] M. Guo, F. Böttcher, J. Hertkorn, J.-N. Schmidt, M. Wenzel, H. P. Büchler, T. Langen, and T. Pfau, Nature (London) **574**, 386 (2019).

[20] G. Natale, R. M. W. van Bijnen, A. Patscheider, D. Petter, M. J. Mark, L. Chomaz, and F. Ferlaino, Phys. Rev. Lett. **123**, 050402 (2019).

[21] I. Ferrier-Barbut, M. Wenzel, F. Böttcher, T. Langen, M. Isoard, S. Stringari, and T. Pfau, Phys. Rev. Lett. **120**, 160402 (2018).

[22] L. Tanzi, J. G. Maloberti, G. Biagioni, A. Fioretti, C. Gabbanini, and G. Modugno, Science **371**, 1162 (2021).

[23] M. A. Norcia, E. Poli, C. Politi, L. Klaus, T. Bland, M. J. Mark, L. Santos, R. N. Bisset, and F. Ferlaino, Phys. Rev. Lett. **129**, 040403 (2022).

[24] S. M. Roccuzzo, A. Recati, and S. Stringari, Phys. Rev. A **105**, 023316 (2022).

[25] M. A. Norcia, C. Politi, L. Klaus, E. Poli, M. Sohmen, M. J. Mark, R. N. Bisset, L. Santos, and F. Ferlaino, Nature (Lndon) **596**, 357 (2021).

[26] T. Bland, E. Poli, C. Politi, L. Klaus, M. A. Norcia, F. Ferlaino, L. Santos, and R. N. Bisset, Phys. Rev. Lett. **128**, 195302 (2022).

[27] A. Gallemí, S. M. Roccuzzo, S. Stringari, and A. Recati, Phys. Rev. A **102**, 023322 (2020).

[28] F. Ancilotto, M. Barranco, M. Pi, and L. Reatto, Phys. Rev. A **103**, 033314 (2021).

[29] Y. Pomeau and S. Rica, Phys. Rev. Lett. **72**, 2426 (1994).

[30] A. R. P. Lima and A. Pelster, Phys. Rev. A **86**, 063609 (2012).

[31] F. Wächtler and L. Santos, Phys. Rev. A **93**, 061603(R) (2016).

[32] L. Klaus, T. Bland, E. Poli, C. Politi, G. Lamporesi, E. Casotti, R. N. Bisset, M. J. Mark, and F. Ferlaino, Nat. Phys. **18**, 1453 (2022).

[33] Z. Hadzibabic, Nat. Phys. **18**, 1393 (2022).

XUV-driven plasma switch for THz: new spatio-temporal overlap tool for XUV–THz pump–probe experiments at FELs[1]

E. Zapolnova,[a] R. Pan,[a] T. Golz,[a] M. Sindik,[a] M. Nikolic,[a] M. Temme,[a] M. Rabasovic,[b] D. Grujic,[b] Z. Chen,[c] S. Toleikis[a] and N. Stojanovic[a]*

[a]Deutsches Elektronen-Synchrotron (DESY), Notkestrasse 85, 22607 Hamburg, Germany, [b]Institute of Physics Belgrade, Pregrevica 118, 11080 Belgrade, Serbia, and [c]SLAC National Accelerator Laboratory, Menlo Park, CA 94025, USA. *Correspondence e-mail: nikola.stojanovic@desy.de

A simple and robust tool for spatio-temporal overlap of THz and XUV pulses in in-vacuum pump–probe experiments is presented. The technique exploits ultrafast changes of the optical properties in semiconductors (*i.e.* silicon) driven by ultrashort XUV pulses that are probed by THz pulses. This work demonstrates that this tool can be used for a large range of XUV fluences that are significantly lower than when probing by visible and near-infrared pulses. This tool is mainly targeted at emerging X-ray free-electron laser facilities, but can be utilized also at table-top high-harmonics sources.

1. Introduction

Intense THz pulses combined with synchronized X-ray pulses enable investigation of the dynamics of the light–matter interaction, non-linear response of materials and control of the properties of matter selectively on femtosecond time scales. Therefore, achieving the temporal overlap between pump and probe pulses in the femtosecond range is essential. Certain pump–probe schemes, *e.g.* THz streaking (Frühling *et al.*, 2009; Schmid *et al.*, 2019), are comparatively tolerant against the spatial overlap between XUV and THz pulses and the actual focal position of the THz beam. The observable, *i.e.* the kinetic energy of the photoelectrons, is furthermore of considerable magnitude and can be utilized for further optimization of the pump–probe signal. This is almost never the case in pump–probe experiments on solid-state samples, utilizing one of the XUV probing techniques [*e.g.* X-ray magnetic circular dichroism (XMCD) (Pfau *et al.*, 2012; Willems *et al.*, 2015) and resonant inelastic X-ray scattering (Dell'Angela *et al.*, 2016)]. There, the spatio-temporal overlap between THz and XUV and in particular diffraction-limited focusing of the THz beam have to be achieved with the aid of versatile in-vacuum diagnostics.

The so-called plasma-switch, the transient change of optical constants in the visible (VIS) and near-infrared (NIR) spectral ranges by X-ray and XUV pulses, has been used for the temporal characterization of these pulses (Harmand *et al.*, 2012; Gahl *et al.*, 2008; Krupin *et al.*, 2012; Riedel *et al.*, 2013; Danailov *et al.*, 2014). Transient changes of optical properties in the THz range, driven by femtosecond laser pulses, have been used for pickup of individual pulses from MHz trains at infrared free-electron lasers (FELs) (Schmidt *et al.*, 2015) as well as for THz spectral shaping at table-top THz sources (Cartella *et al.*, 2014; Mayer *et al.*, 2014).

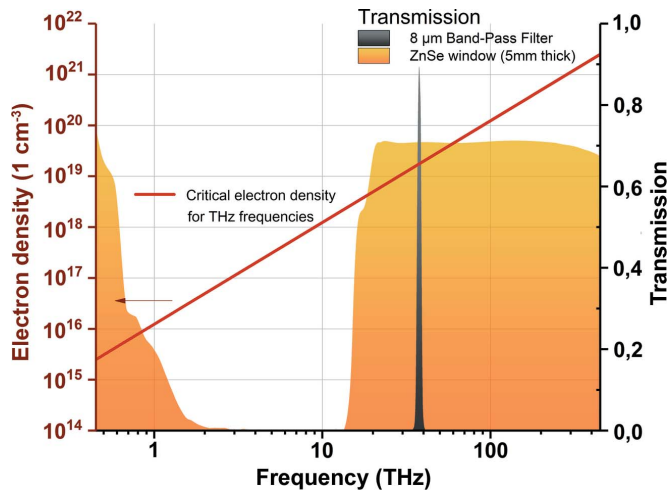https://doi.org/10.1107/S1600577519014164 **11**
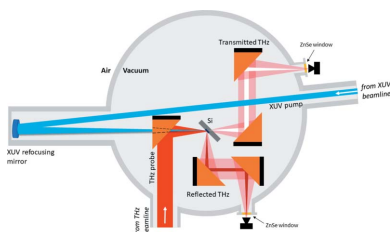
Figure 1
Calculation of the critical electron density for the THz range (red line).
Transmission of the 5 mm-thick ZnSe vacuum window and the bandpass
filter (at 8 μm wavelength) used in the experiment are presented as the
shadowed areas.

As shown in Fig. 1, for lower probing frequencies the effect
of the plasma switch is more efficient because lower electron
density is required to change the material reflectivity. In this
work we present a technique to establish the temporal overlap
between XUV and THz pulses, based on the transient change
of optical properties of a silicon target in the THz spectral
range, induced by the intense femtosecond XUV pulse.

The presented method can be applied in facilities employing
THz radiation for time-resolved XUV–THz pump–probe
experiments where it is necessary to temporally overlap XUV
and THz pulses on a sub-picosecond level.

2. XUV driven THz plasma switch: theoretical background

The process of electronic excitation of materials by an intense
XUV pulse happens on an ultrafast time scale, within a few
femtoseconds (Gahl *et al.*, 2008; Riedel *et al.*, 2013), and is
governed by the photoionization of the electrons in the
material: photoabsorption of the bound electrons within the
valence band, secondary processes as elastic and inelastic
scattering of free electrons, Auger decay, and electron pair
creation. Other processes may contribute to the photo-
ionization depending on the energy of the incoming photon
and the material (Medvedev & Rethfeld, 2010). Previous
theoretical studies have shown that the density of the created
free electrons follows the photon flux of the XUV pulse
linearly (Riedel *et al.*, 2013) in a wide intensity range, below
fluences required for the sample melting, ablation and plasma
formation.

Optical properties of the photo-excited material strongly
depend on the density of free electrons and can be modelled
[*e.g.* via the continuity equation (Mezentsev *et al.*, 2007)] and
expressed in terms of relative permittivity. According to the
Drude model, free electrons in a material can be treated as
free-electron plasma with a corresponding plasma frequency

ω_p (Ashcroft & Mermin, 1976). We assume that the damping
can be neglected in our case (refer to Appendix *A* for a short
discussion on this topic) and the relative permittivity ε in this
case can be presented as a function of the incoming frequency
ω and the plasma frequency ω_p,

$$\varepsilon(\omega) = 1 - \frac{\omega_p^2}{\omega^2}.$$

This indicates that light with a higher frequency than the
plasma frequency, $\omega > \omega_p$, can penetrate the plasma whereas
light with lower frequency, $\omega < \omega_p$, will be reflected. Taking
into account the oscillatory motion of the electron, the critical
electron density, n_e, required to make the sample reflective to
light with a certain frequency can be presented as

$$n_e = \frac{\varepsilon_0 \, m_e}{e^2} \, \omega_p^2,$$

where ε_0 is the vacuum permittivity, e is the charge and m_e is
the mass of an electron.

In our experiment, the critical electron density for the
probing pulse at a wavelength of 8 μm (37.5 THz) is
$n_{e\,8\mu m} = 1.8 \times 10^{19}$ cm^{-3}, and at wavelengths over 100 μm
(<3 THz) it is less than $n_{e\,100\mu m} = 1.1 \times 10^{17}$ cm^{-3}.

3. Description of the setup

The experiment was performed with the pump XUV wave-
length at 13.5 nm (91.8 eV) and two different probing condi-
tions: (i) a THz pulse with a central wavelength of 8 μm, and
(ii) a broadband THz pulse with a wavelength >100 μm. The
expected pulse duration for THz was ~300 fs and ~3 ps,
respectively, and the XUV pulse duration was 160 fs, esti-
mated by electron bunch length measurements by a transverse
deflecting RF-structure (Düsterer *et al.*, 2014).

The THz beam is collimated using five toroidal mirrors in
order to keep the beam size within the range of the beam
transport and optics. This additional folding of the THz beam
results in a ~6.5 m longer optical path with respect to the
XUV beam. In order to overlap the XUV and THz pulses in
time, an additional delay for the XUV is introduced: pulses
travel 3.25 m longer distance and then are refocused by a
mirror with 3.5 m focal length back to the experiment (Pan *et
al.*, 2019). The scheme of the experiment is presented in Fig. 2.

The THz and XUV pulses are collinearly focused and
spatially overlapped in the experimental chamber on a
400 μm-thick Si sample at a 45° incident angle. The trans-
mitted and reflected portions of the THz beam are picked up
and collimated using parabolic mirrors. Then they are focused
through ZnSe vacuum windows (5 mm thick) on two 2 mm ×
2 mm pyro detectors (InfraTec LME-301) located outside of
the experimental chamber in air ~5 mm from the window.
The detectors were custom-designed by collaboration of the
DESY FLA group and InfraTec to reduce internal THz
interferences (Wesch, 2012). The detectors are without optical
windows, which makes them suitable for measurements along
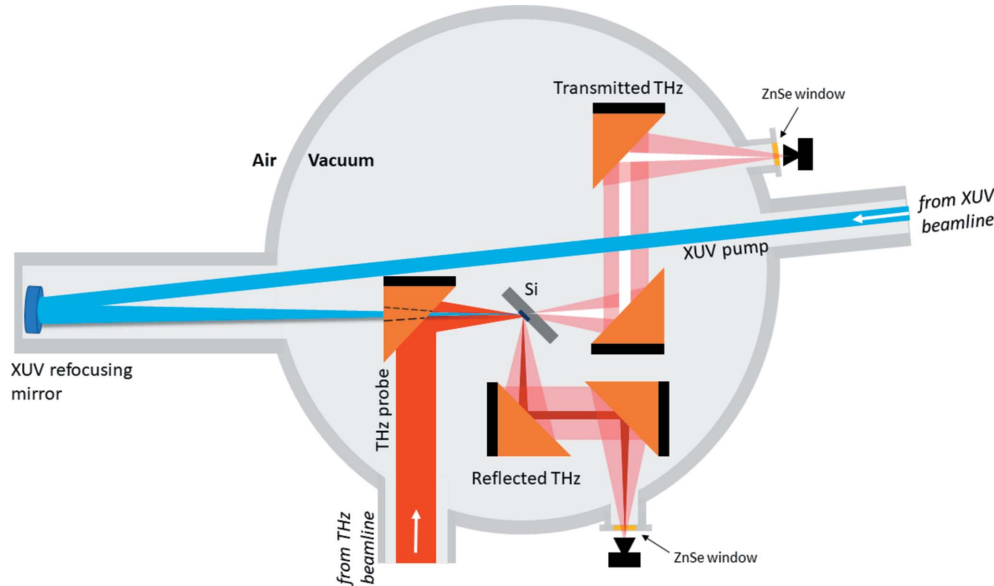a broad spectral range and sensitive to XUV radiation. ZnSe

Figure 2
Scheme of the XUV-driven plasma switch experiment for the THz beam. The THz and XUV beams are collinearly focused and spatially overlapped on a 400 μm-thick Si sample at a 45° incidence angle. Transmitted and reflected THz beams are picked up by off-axis parabolic mirrors and further focused on the corresponding pyro detectors through 5 mm-thick ZnSe vacuum windows.

Table 1
Transmission of XUV at 13.5 nm.

XUV pulse energy via GMD	112 μJ ± 17 μJ
Beamline transmission	78%
Refocusing mirror	62%
Si_3N_4 500 nm filter transmission	1.3%
Total transmission	700 nJ ± 10 nJ

vacuum windows have good transmission in the VIS to IR range as well as in the long-THz wavelength range (see Fig. 1).

Pulse energies of the XUV, measured with the gas-monitor detector (GMD), were 110 μJ ± 20 μJ (r.m.s.) (Tiedtke *et al.*, 2009) and 0.5 μJ ± 0.1 μJ (r.m.s.) for the THz beam measured with a calibrated pulse energy meter (Zapolnova *et al.*, 2018; Pan *et al.*, 2019).

The estimated XUV pulse energy through the beamline (Tiedtke *et al.*, 2009) after the refocusing mirror and through attenuation filters was 700 nJ ± 10 nJ (refer to Table 1 for details), yielding a final intensity on the sample of 6.76×10^9 W cm^{-2} and 2.65×10^9 W cm^{-2}, for the two measured XUV beam sizes (see Section 4 for details). By measuring both transmitted and reflected intensities of the THz beam and assuming that absorption in the excited Si layer is negligible, we are able to correct the pulse-to-pulse energy fluctuations of the THz beam (3.6% RMS at 100 μm, 14% RMS at 8 μm).

4. THz and XUV 2D beam profile

The THz and XUV beams were characterized by 2D profile measurements in the focal position. A pyro detector with a 100 μm pinhole was mounted on an *xy* positioner, facing the incoming THz and XUV beams at normal incidence, and was moved through the focus of the beam with defined steps along the *z* axis. The pyro detector also showed a good response for XUV radiation, and therefore it was used for both the THz and XUV beam profile characterizations.

The results of 2D scans are presented in Fig. 3. The THz beam in focus has an ellipsoidal profile, elongated in the vertical direction, because of imperfect alignment of the off-axis parabolic mirror for the THz beam. The full width at half-maximum (FWHM) diameter of the THz beam with the THz undulator set at a 100 μm nominal wavelength was 400 ± 20 μm × 1470 ± 30 μm, and at 8 μm it was 180 ± 15 μm × 320 ± 15 μm. In an attempt to match the XUV and THz beam sizes we inserted a pinhole (3 mm diameter) in the XUV beam, 30 m upstream of the experiment, to optimize the ratio between beam sizes. The FWHM diameters of the XUV beam with and without a pinhole were 230 ± 30 μm and 140 ± 20 μm, respectively. The ratio between the areas of the THz and XUV beams was 1:9 for the THz beam at 100 μm and 2:3 at 8 μm.

5. Transient reflectivity and transmission

Results of time-dependent reflectivity measurements [presented as $(R - R_0)/R_0$, where R_0 is the equilibrium reflectivity] are presented in Fig. 4. Once the probing THz pulse arrives following the XUV pulse, a portion of the THz pulse, which spatially overlaps with the XUV pulse, is reflected more because of the plasma created by the XUV pulse. The observed duration of the transition (slope) $\Delta\tau_{\lambda_{THz}}$ is the convolution of the pulse durations of the THz $\Delta\tau_{THz}$ and XUV pulses $\Delta\tau_{XUV}$, the jitter $\Delta\tau_{jitter}$ between them, and the timescale of the free carrier excitation process $\Delta\tau_{excitation}$, and can be described as
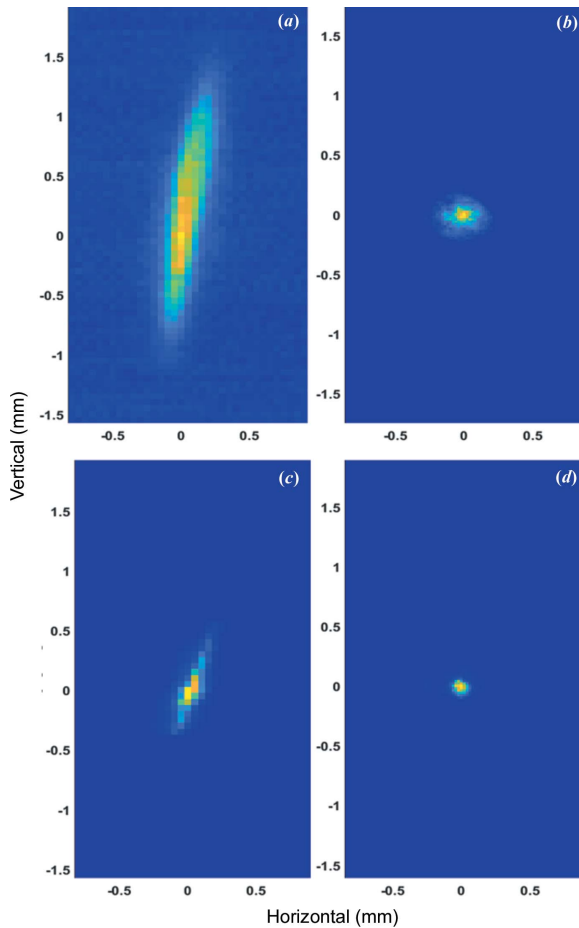
Figure 3
Measured 2D profiles of the THz and XUV beams. (*a*) THz beam profile at 100 µm with an FWHM of 400 ± 20 µm × 1470 ± 30 µm. (*b*) XUV beam at 13.5 nm wavelength through a 3 mm pinhole placed ∼30 m upstream of the experiment with an FWHM of 230 ± 30 µm. (*c*) THz beam profile at 8 µm wavelength with an FWHM of 180 ± 15 µm × 320 ± 15 µm. (*d*) XUV beam at 13.5 nm wavelength with a 10 mm pinhole at the same position as in (*b*) with an FWHM of 140 ± 20 µm.

$$\Delta\tau_{\lambda_{THz}} = \left(\Delta\tau_{THz}^2 + \Delta\tau_{XUV}^2 + \Delta\tau_{jitter}^2 + \Delta\tau_{excitation}^2\right)^{1/2}.$$

For a THz wavelength of ∼100 µm, the observed slope width is $\Delta\tau_{100\mu m} = 2.2$ ps and for 8 µm wavelength it is $\Delta\tau_{8\mu m} = 1.2$ ps (calculated as the time between the points corresponding to the 10% and 90% levels of total amplitude of the signal). The XUV and THz pulses are naturally synchronized in this experiment, with jitter smaller than 5 fs (RMS) (Frühling *et al.*, 2009), and its contribution is negligible. We assume that the excitation of the free carriers is much faster than other time-scales in the experiment so we neglect it as well.

6. Dependence on the XUV fluence

Fig. 5 shows a comparison of the transient THz reflectivity change for different fluences of the pump XUV pulse. We used different combinations of the attenuation filters: Si_3N_4 350 nm (red line), Si_2N_4 350 nm + Nb 405 nm (orange line) and Si_3N_4 500 nm (green line). The effect of the plasma switch in
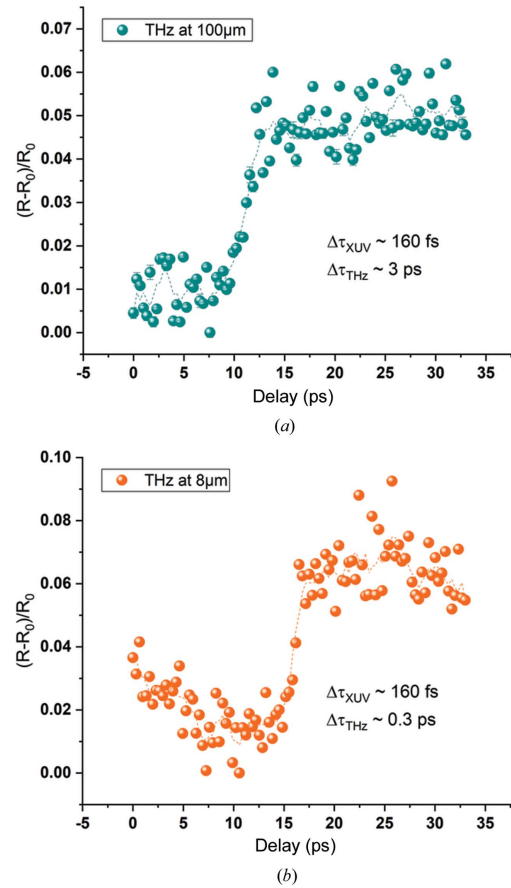

Figure 4
Transient optical reflectivity curves for the THz undulator set at 100 µm and 8 µm wavelengths for a 13.5 nm XUV pump wavelength.

the THz spectral range is very efficient and can be clearly observed even at XUV fluences as low as 45 µJ cm^{-2}.

7. Quantitative estimate of the effect

The amplitude of the reflectivity change for a broadband THz beam >100 µm is around 6.4% and for 8 µm is around 6.0%. Using the details of the actual THz and XUV beam sizes
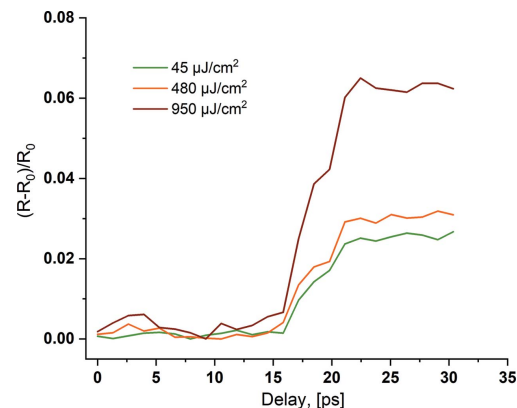

Figure 5
Transient THz reflectivity curves as a function of the THz/XUV pulse delay for three different fluences of the XUV pulse on the sample.

from the 2D profile measurements, we can estimate the actual switched fraction of the THz pulse. Comparing total areas of the beams and assuming that the electron density follows the intensity envelope of the XUV beam linearly, we can assume that, if the XUV beam size matches the size of the THz beams for a 100 μm wavelength (400 μm FWHM beam size) and for a 8 μm wavelength (180 μm FWHM beam size), the overall effect on the reflectivity change would be 9 times higher (∼57.6%) and 1.5 times higher (∼10%) than observed.

8. Summary

We have developed a tool for temporal and spatial overlap of XUV and THz pulses in pump–probe experiments, based on an XUV plasma switch for the THz range on an Si sample. During several pump–probe experiments at FLASH, it was demonstrated that the arrival time of XUV and THz pulses can be established down to at least the pulse duration of the THz pulse.

The experiment has been performed at different XUV fluences from 0.045 mJ cm^{-2} up to 0.95 mJ cm^{-2} for 8 μm wavelength and for the broadband >100 μm wavelength of the probe pulse. The observed change of the transient normalized reflectivity $(R - R_0)/R_0$ of THz beam due to the plasma switch is approximately 6% from the initial level.

Since this effect uses low XUV fluences, far below the damage threshold, and uses room-temperature broadband THz detectors, it is robust and simple. This technique can be further applied at facilities employing XUV–THz pump–probe experiments, and enables a straightforward and efficient method for temporal overlap of XUV and THz pulses on the picosecond time scale.

APPENDIX *A*
Comparison of the excited-layer thickness with the penetration depth of THz radiation

The frequency-dependent dielectric constant, according to the simple Drude model, where damping is independent of the free electron energy, can be expressed as (Van Exter & Grischkowsky, 1990)

$$\varepsilon(\omega) = \varepsilon(\infty) - \frac{\omega_{\mathrm{p}}^2}{\omega(\omega + i\Gamma)},$$

where ω_{p} is the plasma frequency, $\Gamma = 1/\tau_{\mathrm{c}}$ is the damping frequency and τ_{c} is the average free-electron collision time. From the literature, we estimate the average free-electron collision time to be between 1 fs and 100 fs (Ashcroft & Mermin, 1976; Temnov *et al.*, 2006; Van Exter & Grischkowsky; 1990; Riedel *et al.*, 2013). Finally, this gives us the estimated minimum penetration depth for probing THz frequencies (2–40 THz) in XUV-excited plasma in silicon to be ≥2 μm.

For an XUV wavelength of 13.5 nm impinging at a 45° angle of incidence, the thickness of the excited area in silicon is 400 nm, as determined by the penetration depth (Henke *et al.*,

1993). The XUV pulses from FLASH, used in this work (as presented in Fig. 5), result in free-electron densities in the range from 1.2×10^{17} cm^{-3} up to 2.8×10^{18} cm^{-3}.

This leads to the conclusion that only a small fraction of the probing THz radiation (<20%) is absorbed in the investigated sample excited by the XUV pulse.

References

Ashcroft, N. W. & Mermin, D. N. (1976). *Solid State Physics*. New York: Holt, Rinehart and Winston.

Cartella, A., Bonora, S., Först, M., Cerullo, G., Cavalleri, A. & Manzoni, C. (2014). *Opt. Lett.* **39**, 1485–1488.

Danailov, M. B., Bencivenga, F., Capotondi, F., Casolari, F., Cinquegrana, P., Demidovich, A., Giangrisostomi, E., Kiskinova, M. P., Kurdi, G., Manfredda, M., Masciovecchio, C., Mincigrucci, R., Nikolov, I. P., Pedersoli, E., Principi, E. & Sigalotti, P. (2014). *Opt. Express*, **22**, 12869–12879.

Dell'Angela, M., Hieke, F., Malvestuto, M., Sturari, L., Bajt, S., Kozhevnikov, I. V., Ratanapreechachai, J., Caretta, A., Casarin, B., Glerean, F., Kalashnikova, A. M., Pisarev, R., Chuang, Y. D., Manzoni, G., Cilento, F., Mincigrucci, R., Simoncig, A., Principi, E., Masciovecchio, C., Raimondi, L., Mahne, N., Svetina, C., Zangrando, M., Passuello, R., Gaio, G., Prica, M., Scarcia, M., Kourousias, G., Borghes, R., Giannessi, L., Wurth, W. & Parmigiani, F. (2016). *Sci. Rep.* **6**, 1–8.

Düsterer, S., Rehders, M., Al-Shemmary, A., Behrens, C., Brenner, G., Brovko, O., DellAngela, M., Drescher, M., Faatz, B., Feldhaus, J., Frühling, U., Gerasimova, N., Gerken, N., Gerth, C., Golz, T., Grebentsov, A., Hass, E., Honkavaara, K., Kocharian, V., Kurka, M., Limberg, Th., Mitzner, R., Moshammer, R., Plönjes, E., Richter, M., Rönsch-Schulenburg, J., Rudenko, A., Schlarb, H., Schmidt, B., Senftleben, A., Schneidmiller, E. A., Siemer, B., Sorgenfrei, F., Sorokin, A. A., Stojanovic, N., Tiedtke, K., Treusch, R., Vogt, M., Wieland, M., Wurth, W., Wesch, S., Yan, M., Yurkov, M. V., Zacharias, H. & Schreiber, S. (2014). *Phys. Rev. ST Accel. Beams*, **17**, 120702.

Exter, M. van & Grischkowsky, D. (1990). *Phys. Rev. B*, **41**, 12140–12149.

Frühling, U., Wieland, M., Gensch, M., Gebert, T., Schütte, B., Krikunova, M., Kalms, R., Budzyn, F., Grimm, O., Rossbach, J., Plönjes, E. & Drescher, M. (2009). *Nat. Photon.* **3**, 523–528.

Gahl, C., Azima, A., Beye, M., Deppe, M., Döbrich, K., Hasslinger, U., Hennies, F., Melnikov, A., Nagasono, M., Pietzsch, A., Wolf, M., Wurth, W. & Föhlisch, A. (2008). *Nat. Photon.* **2**, 165–169.

Harmand, M., Murphy, D., Brown, D., Cammarata, M., Döppner, T., Düsterer, S. & Toleikis, S. (2012). *J. Instrum.* **7**, P08007.

Henke, B. L., Gullikson, E. M. & Davis, J. C. (1993). *Atom Data Nucl. Data*, **54**, 181–342.

Krupin, O., Trigo, M., Schlotter, W. F., Beye, M., Sorgenfrei, F., Turner, J. J. & Wurth, W. (2012). *Opt. Express*, **20**, 11396–11406.

Mayer, B., Schmidt, Ch., Bühler, J., Seletskiy, D. V., Brida, D., Pashkin, A. & Leitenstorfer, A. (2014). *New J. Phys.* **16**, 063033.

Medvedev, N. & Rethfeld, B. (2010). *New J. Phys.* **12**, 73037.

Mezentsev, V., Petrovic, J. S., Dubov, M., Bennion, I., Dreher, J., Schmitz, H. & Grauer, R. (2007). *Proc. SPIE*, **6459**, 64590B.

Pan, R., Zapolnova, E., Golz, T., Krmpot, A. J., Rabasovic, M. D., Petrovic, J., Asgekar, V., Faatz, B., Tavella, F., Perucchi, A., Kovalev, S., Green, B., Geloni, G., Tanikawa, T., Yurkov, M., Schneidmiller, E., Gensch, M. & Stojanovic, N. (2019). *J. Synchrotron Rad.* **26**, 700–707.

Pfau, B., Schaffert, S., Müller, L., Gutt, C., Al-Shemmary, A., Büttner, F., Delaunay, R., Düsterer, S., Flewett, S., Frömter, R., Geilhufe, J., Guehrs, E., Günther, C. M., Hawaldar, R., Hille, M., Jaouen, N., Kobs, A., Li, K., Mohanty, J., Redlin, H., Schlotter, W. F., Stickler, D., Treusch, R., Vodungbo, B., Kläui, M., Oepen, H. P., Lüning, J., Grübel, G. & Eisebitt, S. (2012). *Nat. Commun.* **3**, 1100.

Riedel, R., Al-Shemmary, A., Gensch, M., Golz, T., Harmand, M., Medvedev, N., Prandolini, M. J., Sokolowski-Tinten, K., Toleikis, S., Wegner, U., Ziaja, B., Stojanovic, N. & Tavella, F. (2013). *Nat. Commun.* **4**, 1731–1737.

Schmid, G., Schnorr, K., Augustin, S., Meister, S., Lindenblatt, H., Trost, F., Liu, Y., Stojanovic, N., Al-Shemmary, A., Golz, T., Treusch, T., Gensch, M., Kübel, M., Foucar, L., Rudenko, A., Ullrich, J., Schröter, C. D., Pfeifer, T. & Moshammer, R. (2019). *Phys. Rev. Lett.* **122**, 073001.

Schmidt, J., Winnerl, S., Seidel, W., Bauer, C., Gensch, M., Schneider, H. & Helm, M. (2015). *Rev. Sci. Instrum.* **86**, 063103.

Temnov, V. V., Sokolowski-Tinten, K., Zhou, P., El-Khamhawy, A. & von der Linde, D. (2006). *Phys. Rev. Lett.* **97**, 237403.

Tiedtke, K., Azima, A., Von Bargen, N., Bittner, L., Bonfigt, S., Düsterer, S., Faatz, B., Frühling, U., Gensch, M., Gerth, Ch., Gerassimova, N., Hahn, U., Hesse, M., Honkavaara, K., Jastrow, U., Juranic, P., Kapitzki, S., Keitel, B., Kracht, T., Kuhlman, M., Li, W. B., Martins, M., Nuñez, T., Plönjes, E., Redlin, H., Saldin, E. L., Schneidmiller, E. A., Schneider, J. R., Schreiber, S., Stojanovic, N., Tavella, F., Toleikis, S., Treusch, R., Weigelt, H., Wellhöfer, M., Wabnitz, H., Yurkov, M. V. & Feldhaus, J. (2009). *New J. Phys.* **11**, 023029.

Wesch, S. (2012). Dissertation. DESY, Hamburg, Germany.

Willems, F., Smeenk, C. T. L., Zhavoronkov, N., Kornilov, O., Radu, I., Schmidbauer, M., Hanke, M., von Korff Schmising, C., Vrakking, M. J. J. & Eisebitt, S. (2015). *Phys. Rev. B*, **92**, 220405.

Zapolnova, E., Golz, T., Pan, R., Klose, K., Schreiber, S. & Stojanovic, N. (2018). *J. Synchrotron Rad.* **25**, 39–43.

Rapid Communications

Periodic three-body orbits in the Coulomb potential

Marija Šindik,[1] Ayumu Sugita,[2] Milovan Šuvakov,[3] and V. Dmitrašinović[3,*]

[1]*Faculty of Physics, University of Belgrade, Studentski Trg 12, 11000 Belgrade, Serbia*
[2]*Department of Applied Physics, Osaka City University, 3-3-138 Sugimoto, Sumiyoshi-ku, Osaka 558-8585, Japan*
[3]*Institute of Physics Belgrade, University of Belgrade, Pregrevica 118, Zemun, 11080 Belgrade, Serbia*

We numerically discovered around 100 distinct nonrelativistic collisionless periodic three-body orbits in the Coulomb potential *in vacuo*, with vanishing angular momentum, for equal-mass ions with equal absolute values of charges. These orbits are classified according to their symmetry and topology, and a linear relation is established between the periods, at equal energy, and the topologies of orbits. Coulombic three-body orbits can be formed in ion traps, such as the Paul, or the Penning one, where one can test the period vs topology prediction.

The Newtonian three-body problem is one of the outstanding classical open questions in science. After more than 300 years of observation, only two topologically distinct types of periodic three-body systems, or orbits, have been observed in the skies [1]: (1) the so-called hierarchical systems, such as the Sun-Earth-Moon one, to which type belong more than 99% of all observed three-body systems; (2) Lagrangian three-body systems, such as Jupiter's Trojan satellites, to which the remaining ⩽1% belong.

There has been some significant theoretical progress on the subject over the past few years: several hundred new, topologically distinct families of periodic solutions have been found by way of numerical simulations [2–16], and unexpected regularities have been observed among them [9,13,15,16] relating the periods, topologies, and linear stability of orbits.

Of course, one would like to observe at least some of the new orbits and test their properties in an experiment, but such a test would be impeded by a number of obstacles: (1) only stable orbits have a chance of actually existing for a sufficiently long time to be observed; (2) stability depends on the ratio(s) of masses, and on the value of angular momentum, neither of which can be controlled in astronomical settings; (3) even if an orbit is stable in a wide range of mass ratios and angular momenta, there is no guarantee that such a system will have been formed sufficiently frequently and sufficiently close to Earth, that it may be observed by our present-day instruments.

All of the above prompted us to look for alternative three-body systems that share (at least) some of the same properties with Newtonian three-body systems. The Coulombic potential shares one basic similarity with the Newtonian gravity—its characteristic $1/r$ (homogeneous) spatial dependence—as well as several important differences: (1) the (much) larger coupling constant; (2) both attractive and repulsive nature; (3) naturally identical (quantized) electric charge(s); (4) ions with opposite charges may have masses equal to one part in a few

thousand; (5) ions have a finite probability of elastic scattering in head-on collisions; and (6) Coulombic bound states can be formed in table-top ion-trap experiments [17]. For these reasons we turn to the study of periodic three-body orbits bound by Coulombic potential. The application of only the Coulomb interaction amounts to a nonrelativistic approximation, which is good only in the low-velocity limit [18].

In this Rapid Communication we present the results of a search that led to around 100 distinct collisionless orbits, only four of which are stable, and around 80 isosceles quasicolliding (free-fall, or "brake") ones. We use the collisionless orbits to display a new regularity, akin to Kepler's third law, in the form of a linear dependence

$$T|E|^{3/2} \sim N, \qquad (1)$$

between the scale-invariant period $T|E|^{3/2}$, where T is the period, and E is the energy of an orbit, on one hand, and the orbit's topological complexity N, expressed as the number of collinear configurations ("syzygies") encountered during one cycle (see the text below), on the other. This prediction ought to be tested in ion-trap experiments.

We used the same search method as in the Newtonian gravity three-body problem [5]. There are 12 independent variables that define the initial state of this system; for each body there are the x and y coordinates of the body, and the v_x and v_y components of their velocity. Adopting the center-of-mass reference frame reduces this number (12) to eight. Fixing the value of angular momentum ($L = 0$) reduces this further to six. Using the scaling rules [19] for the solutions and the fact that periodic solution must pass through at least one syzygy (collinear configuration) during one period, yields a four-dimensional search space for all zero-angular-momentum periodic solutions. We search for solutions in the two-dimensional subspace of orbits that pass through the Euler configuration, defined as the symmetric collinear configuration wherein the positively charged particle with velocity $(-2v_x, -2v_y)$ passes through the origin $(0, 0)$, i.e., exactly between the two negatively charged particles, which, in turn, pass through the points $(-1, 0)$ and $(1, 0)$, both with velocity equal to (v_x, v_y).
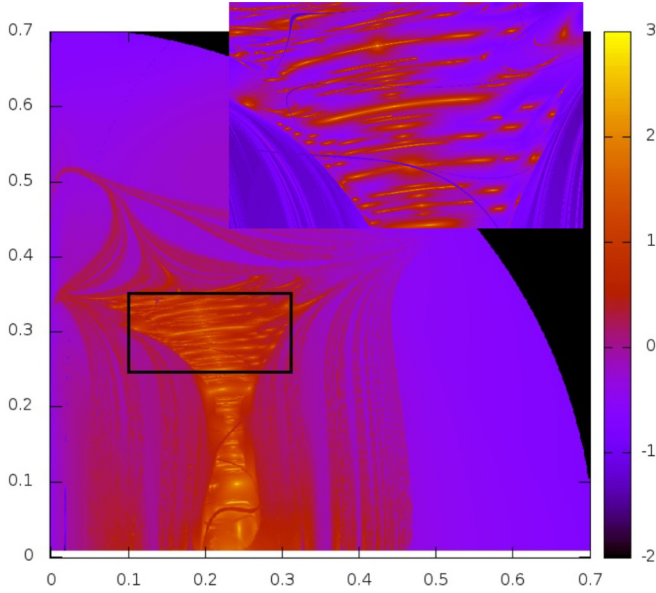
FIG. 1. Negative logarithm of return proximity function as a function of the initial velocity components v_x and v_y on the x and y axes, respectively. Bright areas correspond to high values of the negative logarithm. Inset: zoom-in of the "boxed-in" region.

In order to search for periodic solutions numerically, we have discretized the search window in this two-dimensional subspace and calculated the return proximity function (RPF) $d_{T_0}(v_x, v_y)$ that measures how close to the initial condition the trajectory returns (see [20]) up to some predefined upper limit on the integration time T_0, at each grid point. The negative logarithm of the computed RPF is shown in Fig. 1. Local minima of RPF are used as candidates for periodic solutions. After applying the gradient descent algorithm starting at each candidate point, we have declared as periodic the solutions with RPF of $\mathcal{O}(10^{-8})$ and smaller.

We have followed the example set by three-body orbits in Newtonian gravity [5,13], and classified the newly found Coulombic orbits according to their topologies, studied their stability, and organized them into sequences some of which, although fewer in number, appear very similar to the Newtonian ones. Each orbit has a well-defined topology which can be algebraized in at least two different ways (see [20] and Refs. [21,22]). Here we use Montgomery's method [21] wherein each solution is associated with [the conjugacy class (see [5]), of] an element of the two-generator (a, b, A = a^{-1}, B = b^{-1}) free group F_2(a, b).

There are important distinctions among the 100-odd orbits: (1) the orbits can be separated into two classes, using their symmetry: class A consists of orbits that are symmetrical under two perpendicular reflections, and class B of orbits with a point reflection symmetry; (2) each of the classes can be further separated into sequences, defined by their free-group elements, as follows. For both class A and class B, sequence (I): $w_{n,k}^{(I)} = [(AB)^n(ab)^n]^k$ with integers $n, k = 1, 2, 3, \ldots$; and for class A only, sequence (II): $w_{m,n,k}^{(A,II)} = [(AB)^m(ab)^n]^k A[(BA)^m(ba)^n]^k B$, with $m, n, k = 1, 2, 3, \ldots$; and sequence (III): $w_n^{(III)} = [(ab)^2ABA(ba)^2BAB]^n$, with $n = 1, 2, 3, \ldots$.

Note that the 100-odd collisionless Coulombic orbits are substantially fewer than roughly 200 collisionless Newtonian orbits with similar search parameters, and that there are only four linearly stable solutions in contrast to more than 20 in the Newtonian case.

All of this is a consequence of just one sign change in the potential: one pair of charged particles must experience repulsion, contrary to Newtonian gravity, where all pairs are attractive. Therefore, no choreographic solution, i.e., permutationally symmetric solution with all three particles following the same trajectory, such as the famous "figure-8" orbit, may exist in the Coulombic case. Moreover, at least one orbit, similar to Orlov's [4] colliding "*S* orbit" (in Newtonian gravity) still exists in the Coulombic case, but it is not stable anymore, and consequently does not produce an infinite sequence of periodic orbits (see [13]).

The initial conditions of all 100-odd orbits and their corresponding topological and kinematical properties can be found in [20]; in Fig. 2 and Table I we have shown six representative solutions.

Next we show that Eq. (1), the (striking) property of orbits that was first observed in Newtonian three-body systems [9], also features in the Coulombic three-body systems. This relation between topological and kinematical properties of Newtonian three-body systems was first reported in [9] and later studied in more detail in Refs. [11,13,15,16]. Equation (1) is a (simple) linear dependence of the scale-invariant period $T|E|^{3/2}$ on the topological complexity N. The topological complexity N can be measured in at least two different ways: (1) we used the length N_w of the free-group element (word) describing the orbit's topology, which, due to symmetry in our case, is equal to the number of asymmetric syzygies, i.e., collinear configurations wherein the two equal-charge particles are next to each other, over one period; (2) the number N_e of *all* syzygies (collinear configurations) was considered in Refs. [9,13] as the measure of topological complexity N of Newtonian orbits.

In Fig. 3 one can see that Eq. (1) holds for three-body orbits in the Coulomb potential: (1) with $N = N_w$, a linear fit yields a slope equal to 1.8252, with asymptotic standard error of 0.08% and an average relative deviation of points from fit values that equals 0.63%; (2) with $N = N_e$ the number of *all* syzygies (collinear configurations), in the Coulomb case, the situation is slightly different (see inset in Fig. 3): the slope of this fit is 1.0208, the asymptotic standard error is 0.36%, but with a significantly larger (2.6%) average relative deviation of points from fit values.

As mentioned earlier, only four solutions are linearly stable. We solved the equations for an infinitesimal deviation from the exact periodic solution along each periodic orbit to find the eigenvalues of the monodromy matrix (see [20]). Due to the symmetry of the equations of motion, these eigenvalues appear as two ($i = 1, 2$) quadruples ($\lambda_i, \lambda_i^*, 1/\lambda_i, 1/\lambda_i^*$). For only four orbits listed in Table II both eigenvalues λ_i have moduli equal to unity $|\lambda_i| = 1$, within their respective margins of error, which means that the corresponding three-body orbit is linearly stable.

Thus we have shown that some of the phenomena first observed in Newtonian three-body orbits, such as the linear dependence of the scale-invariant period on the topology
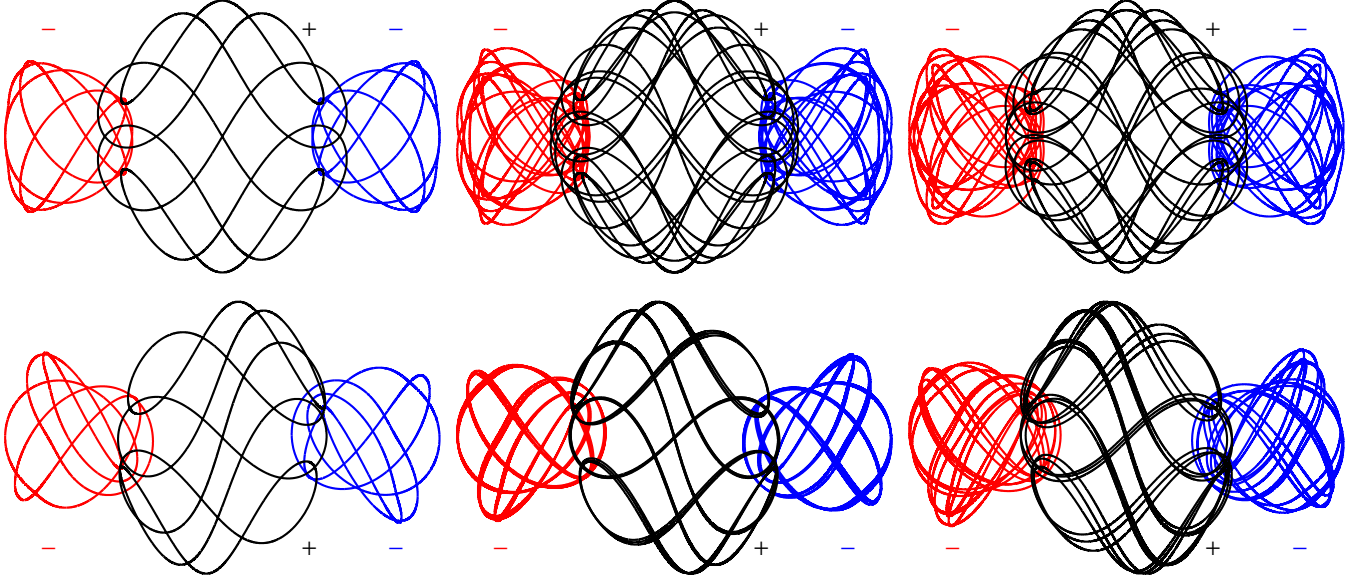
FIG. 2. Trajectories of orbits A.4, with topology $(AB)^2(ab)^2$; A.12.a and A.12.b, both with topology $[(AB)^2(ab)^2]^3$, in class A (upper row); and orbits B.4, with topology $(AB)^2(ab)^2$, and B.12.a and B.12.b, both with topology $[(AB)^2(ab)^2]^3$, in class B (lower row), respectively. Note the independent symmetries of the class A (upper row) trajectories with respect to the reflections about the horizontal and the vertical axis, whereas the class B (lower row) trajectories have only this symmetry under combined reflections. Black lines correspond to the positively charged particle while red and blue lines correspond to the negatively charged ones.

of the orbit, and the emergence of sequences [23] exist in Coulombic three-body orbits, and are not features of Newtonian gravity alone. The homogeneity [19] of the Coulombic, Newtonian, and the strong Jacobi-Poincaré potentials is common to all three known cases of manifestation of this regularity [9,13,25]. This supports indirectly the explanation offered in Refs. [13,25].

Our next concern ought to be the observation of some of these orbits in an experiment. The trajectories of a number (ranging between 1 and 32) of positively charged particles moving in a Paul trap have been photographically recorded as early as 1959 [17,26]. The challenge to actually confine and

photograph a few oppositely charged macroscopic particles in an ion trap has remained unanswered to the present day, to our knowledge. It is well known that Paul and/or Penning traps can lead to binding of pairs of identical ions, including periodic orbits as well as their chaotic motions [27,28], when the circumstances (such as the frequency and amplitudes of the applied electric and/or magnetic fields) are right. Such periodic orbits are impossible in free space, however, as there the identical ions experience only Coulomb repulsion [29]. So, before one observes any periodic three-body orbits in an ion trap, and declares them genuine Coulomb orbits, one must know which periodic three-body orbits exist in free space—

TABLE I. Initial conditions of six orbits, depicted in Fig. 2, that belong to the sequence described by the free-group elements $[(AB)^2(ab)^2]^k$, with $k = 1, 2, 3, \ldots$, and four linearly stable orbits, Table II. The columns correspond to solution label, name of the sequence that the solution belongs to, initial velocities [$\dot{x}_1(0)$ and $\dot{y}_1(0)$], period, negative energy, scaled period, free-group element, number of letters in free-group element (equal to the number of asymmetric syzygies), and the total number of syzygies over a period. For initial conditions of all other found solutions, see [20].

| Label	Seq.	$\dot{x}_1(0)$	$\dot{y}_1(0)$	T	$-E$	$T\|E\|^{3/2}$	Free-group element	N_w	N_e
A.4	I	0.191764	0.330958	13.4332	1.06108	14.6826	$(AB)^2(ab)^2$	8	14
A.12.a	I	0.147917	0.323693	37.1599	1.12003	44.0473	$[(AB)^2(ab)^2]^3$	24	42
A.12.b	I	0.246251	0.335527	45.3784	0.980345	44.0472	$[(AB)^2(ab)^2]^3$	24	42
B.4	I	0.111427	0.305087	11.3981	1.18352	14.6755	$(AB)^2(ab)^2$	8	14
B.12.a	I	0.327539	0.337033	57.4554	0.83738	44.0266	$[(AB)^2(ab)^2]^3$	24	42
B.12.b	I	0.345214	0.344247	63.0644	0.786962	44.0266	$[(AB)^2(ab)^2]^3$	24	42
A.15.b	II	0.108065	0.323579	44.7536	1.15086	55.2534	$(ab)^2ABA(ba)^2bABA$		
							$\times(ba)^2BAB(ab)^2aBAB$	30	52
A.18	III	0.105224	0.336995	55.6513	1.12609	66.5019	$(ab)^2ABA(ba)^2(BA)^2bab$		
							$\times(AB)^2aba(BA)^2(ba)^2BAB$	36	62
A.20.b	I	0.126494	0.315968	59.3293	1.15249	73.4049	$[(ab)^2(AB)^2]^5$	40	70
A.24.a	II	0.249577	0.291337	80.2223	1.0585	87.364	$[(ab)^2(AB)^2A]^2(ba)^2b$		
							$\times(AB)^2[(ab)^2a(BA)^2B]^2$	48	86
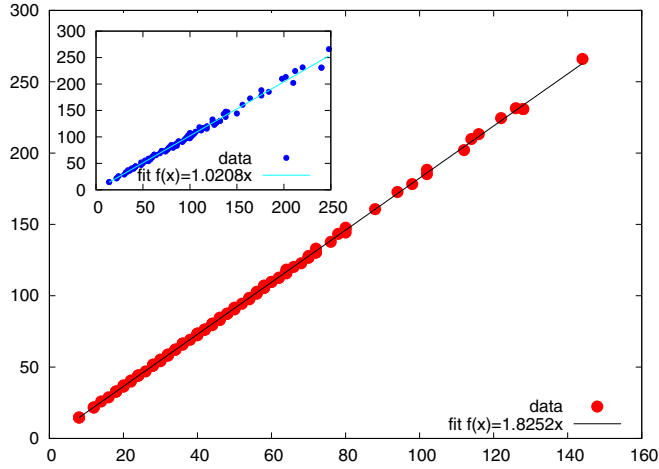
FIG. 3. Dependence of the scale-invariant period $T|E|^{3/2}$ on the number of asymmetric syzygies N_w (collinear configurations with two particles of the same charge on one side) during an orbit. Inset: dependence of the scale-invariant period $T|E|^{3/2}$ on the number of all syzygies N_e.

TABLE II. Stability coefficients λ_j, ν_j, with $j = 1, 2$, of linearly stable (double elliptic) orbits, where $\lambda_j = \exp(2\pi i \nu_j)$.

Name	Re(λ_i)	Im(λ_i)	$|\lambda_i|^2$	ν_i	N_w
A.15.b	0.510145	0.860102	1.000023	0.164797	30
A.15.b	− 0.11507	0.993357	0.999999	0.268355	30
A.18	− 0.002025	0.999961	0.999926	0.250322	36
A.18	− 0.820340	0.571882	1.000007	0.403107	36
A.20.b	0.009875	0.998966	0.998031	0.248427	40
A.20.b	0.94189	0.339728	1.002572	0.055094	40
A.24.a	− 0.988601	0.174067	1.007631	0.472261	48
A.24.a	0.993975	0.116863	1.001643	0.018627	48

information that we have provided here. With the present work we have prepared the terrain for future numerical, and we hope also experimental studies of three-ion motions in traps [17].

Naturally, the orbits that are (linearly) stable in free space are also expected to exist in a trap; that is not to say that the unstable orbits cannot be stabilized by appropriate trapping fields, or that new kinds of periodic orbits cannot be formed in a trap. Moreover, ions have a nonzero elastic head-on collision cross section, unlike the stars and/or planets, so one may even observe some "colliding" orbits [31] in ion traps. This gives one an opportunity to observe hitherto experimentally unobserved orbits and to study some of their unprecedented properties.

At any rate, trap-induced corrections will have to be calculated for each three-ion orbit in any trap where experiments are conducted, before an interpretation is given. With this Rapid Communication we hope to start a discussion of trap-induced corrections for periodic three-ion orbits: in order to calculate such corrections, one needs the (initial conditions of) free-space periodic orbits, of which we have provided around 100, which ought to suffice for a starting point.

There are no records, to our knowledge, of searches for periodic Coulombic three-body systems with equal masses

and equal charges, which are the closest to the equal-mass Newtonian system that was studied in Refs. [4–12,14–16]. As we wished to compare the closest analog of the Coulombic and Newtonian three-body systems, we had to repeat a search for periodic collisionless orbits at the present mass and charge ratios.

To be sure, we are not the first ones who have studied Coulombic periodic three-body motion: the subject has a long history (see, e.g., Refs. [32,33]), with a revival in the 1980s, since when a number of studies have been published: [34–44]. A numerical discovery of more than 8000 collinear colliding periodic orbits with He atom mass ratios was reported in Ref. [39], and of somewhat fewer collisionless ones in Ref. [40]. The initial conditions were not published, so one could not simply retrieve these previously discovered orbits and use them here.

With this Rapid Communication we also hope to induce practitioners to consider experimental searches, particularly in view of the fact that, at least in the case of past periodic-orbit discoveries, the theory did not precede experiment [17].

[1] A. Tokovinin, Dynamics of multiple stars: Observations, in *Massive Stars in Interacting Binaries*, ASP Conference Series Vol. 367, edited by N. St-Louis and A. F. J. Moffat (Astronomical Society of the Pacific, San Francisco, 2007), pp. 615–619.

[2] C. Moore, Braids in Classical Gravity, Phys. Rev. Lett. **70**, 3675 (1993).

[3] A. Chenciner and R. Montgomery, A remarkable periodic solution of the three-body problem in the case of equal masses, Ann. Math. **152**, 881 (2000).

[4] A. I. Martynova, V. V. Orlov, and A. V. Rubinov, Astron. Rep. **53**, 710 (2009).

[5] M. Šuvakov, and V. Dmitrašinović, Three Classes of Newtonian Three-Body Planar Periodic Orbits, Phys. Rev. Lett. **110**, 114301 (2013).

[6] M. Šuvakov, Numerical search for periodic solutions in the vicinity of the figure-eight orbit: Slaloming around singularities on the shape sphere, Celest. Mech. Dyn. Astron. **119**, 369 (2014).

[7] M. Šuvakov, and V. Dmitrašinović, A guide to hunting periodic three-body orbits, Am. J. Phys. **82**, 609 (2014).

[8] M. Šuvakov and M. Shibayama, Three topologically nontrivial choreographic motions of three bodies, Celest. Mech. Dyn. Astron. **124**, 155 (2016).

[9] V. Dmitrašinović and M. Šuvakov, Topological dependence of Kepler's third law for planar periodic three-body orbits with vanishing angular momentum, Phys. Lett. A **379**, 1939 (2015).

[10] P. P. Iasko and V. V. Orlov, Search for periodic orbits in the general three-body problem, Astron. Rep. **58**, 869 (2014).

[11] M. R. Janković and V. Dmitrašinović, Angular Momentum and Topological Dependence of Kepler's Third Law in the Broucke-Hadjidemetriou-Hénon Family of Periodic Three-Body Orbits, Phys. Rev. Lett. **116**, 064301 (2016).

[12] D. Rose, Ph.D. thesis, 'Geometric phase and periodic orbits of the equal-mass, planar three-body problem with vanishing angular momentum', University of Sydney, 2016. Available at https://ses.library.usyd.edu.au/handle/2123/14416

[13] V. Dmitrašinović, A. Hudomal, M. Shibayama, and A. Sugita, Linear stability of periodic three-body orbits with zero angular momentum and topological dependence of Kepler's third law: A numerical test, J. Phys. A: Math. Theor. **51**, 315101 (2018),

[14] http://three-body.ipb.ac.rs/ and http://three-body.ipb.ac.rs/sequences.php

[15] X. Li and S. Liao, More than six hundred new families of Newtonian periodic planar collisionless three-body orbits, Sci. China, Phys. Mech. Astron. **60**, 129511 (2017).

[16] X. Li, Y. Jing, and S. Liao, The 1223 new periodic orbits of planar three-body problem with unequal mass and zero angular momentum, Publ. Astron. Soc. Jpn. **70**, psy057 (2018).

[17] F. G. Major, V. N. Gheorghe, G. Werth, *Charged Particle Traps: Physics and Techniques of Charged Particle Field Confinement*, (Springer, Berlin/Heidelberg, 2005).

[18] L. D. Landau and E. M. Lifshitz, *The Classical Theory of Fields*, 4th revised English ed. (Butterworth-Heinemann, Oxford, 1994).

[19] L. D. Landau and E. M. Lifshitz, Mechanical similarity, in *Mechanics*, 3rd ed. (Butterworth-Heinemann, Oxford, 1976), Sec. 10.

[20] See Supplemental Material at http://link.aps.org/supplemental/10.1103/PhysRevE.98.060101 for periodic three-body orbits in the Coulomb potential, which includes, but is not limited to (a) tables of initial conditions, topologies of orbits; (b) figures of orbits' tajectories; (c) description of the search method; and (d) stability analysis.

[21] R. Montgomery, The *N*-body problem, the braid group, and action-minimizing periodic solutions, Nonlinearity **11**, 363 (1998).

[22] K. Tanikawa and S. Mikkola, Resonances, Stabilization, and Stable Chaos in Hierarchical Triple Systems, edited by V. V. Orlov and A. V. Rubinov (St Petersburg State University Press, St Petersburg, 2008), p. 26.

[23] From a linearly stable orbit, in agreement with the Birkhoff-Lewis theorem [24].

[24] G. D. Birkhoff and D. C. Lewis, On the periodic motions near a given periodic motion of a dynamical system, Ann. Mat. Pura Appl. **12**, 117 (1933).

[25] V. Dmitrašinović, Luka V. Petrović, and M. Šuvakov, Periodic three-body orbits with vanishing angular momentum in the pairwise "strong" potential, J. Phys. A **50**, 435102 (2017).

[26] R. F. Wuerker, H. Shelton, and R. V. Langmuir, Electrodynamic containment of charged particles, J. Appl. Phys. **30**, 342 (1959).

[27] J. Hoffnagle, R. G. DeVoe, L. Reyna, and R. G. Brewer, Order-Chaos Transition of Two Trapped Ions, Phys. Rev. Lett. **61**, 255 (1988).

[28] H. Totsuji, T. Kishimoto, C. Totsuji, and K. Tsuruta, Competition between Two Forms of Ordering in Finite Coulomb Clusters, Phys. Rev. Lett. **88**, 125002 (2002).

[29] Curiously, the case of two opposite-charged, equal-mass ions had not been examined in detail, until recently (see, e.g., [30], although it also falls into the first Mathieu stability zone).

[30] D. Trypogeorgos and C. J. Foot, Cotrapping different species in ion traps using multiple radio frequencies, Phys. Rev. A **94**, 023609 (2016).

[31] We put the word colliding into quotation marks here, because only zero-angular-momentum orbits experience actual collisions, whereas ion traps generally impart (some) angular momentum to ions.

[32] I. Langmuir, The structure of the helium atom, Phys. Rev. **17**, 339 (1921).

[33] G. H. Wannier, The threshold law for single ionization of atoms or ions by electrons, Phys. Rev. **90**, 817 (1953).

[34] I. Davies, A. Truman, and D. Williams, Classical periodic solutions of the equal-mass 2n-body problem, 2n-ion problem, and the n-electron atom problem, Phys. Lett. A **99**, 15 (1983).

[35] H. Klar, Equilibrium Atomic Structure: Rotating Atoms, Phys. Rev. Lett. **57**, 66 (1986).

[36] M. Poirier, Possible rigid rotations in two-electron atoms, Phys. Rev. A **40**, 3498 (1989).

[37] P. Grujić and N. Simonović, The classical helium atom—An asynchronous-mode model, J. Phys. B **24**, 5055 (1991).

[38] K. Richter and D. Wintgen, Stable Planetary Atom Configurations, Phys. Rev. Lett. **65**, 1965 (1990).

[39] K. Richter, G. Tanner, and D. Wintgen, Classical mechanics of two-electron atoms, Phys. Rev. A **48**, 4182 (1993).

[40] T. Yamamoto and K. Kaneko, Helium Atom as a Classical Three-Body Problem, Phys. Rev. Lett. **70**, 1928 (1993).

[41] A. Santander, J. Mahecha, and F. Pérez, Rigid-rotator and fixed-shape solutions to the Coulomb three-body problem, Few-Body Syst. **22**, 37 (1997).

[42] T. J. Stuchi, A. C. B. Antunes, and M. A. Andreu, Muonic helium atom as a classical three-body problem, Phys. Rev. E **62**, 7831 (2000).

[43] M. M. Sano, The classical Coulomb three-body problem in the collinear eZe configuration, J. Phys. A **37**, 803 (2004).

[44] F. Rupp and J. Scheurle, Genuine equilibria of three body Coulomb configurations, Few-Body Syst. **48**, 1 (2010).

Quantized vortices in dipolar BECs when crossing the superfluid-supersolid phase transition

M. Sindik[1,2], A. Recati[1,3], S.M. Roccuzzo[4], L. Santos[5] and S. Stringari[1,3]

[1]*Pitaevskii BEC Center and Department of Physics, University of Trento, Italy*
[2]*Institute of Physics Belgrade, University of Belgrade, Serbia*
[3]*Trento Institute for Fundamental Physics and Applications, INFN, Italy*
[4]*Kirchhoff-Institute for Physics, Ruprecht-Karl University of Heidelberg, Germany*
[5]*Institute for Theoretical Physics, Leibniz Universität Hannover, Germany*
e-mail: marija.sindik@unitn.it

We study quantized vortices in dipolar Bose-Einstein condensates at the transition between the superfluid and the supersolid phase [1]. Recently, ultracold atomic gases have revealed unique features of supersolidity, an intriguing state of matter which presents simultaneously crystalline order and superfluidity [2-4]. However, the experimental observation of quantized vortices in these systems remains an open issue, since their observability in dipolar supersolids is largely prevented by the strong density depletion caused by the formation of droplets [5].

We propose a novel approach to the nucleation of vortices and their observation, based on the quenching of the s-wave scattering length across the phase transition. Starting from a slowly rotating, vortex-free configuration in the superfluid phase, quenching into the supersolid phase drives the vortex nucleation, due to the strong reduction of the critical angular velocity in the supersolid, as illustrated in Fig. 1. Once a vortex is created, it is robustly preserved when the condensate is brought back to the superfluid phase, where it may be readily observed. These results may have a significant impact on ongoing experiments, given that the observation of quantized vortices would constitute a key probe of the superfluid character of dipolar supersolids.
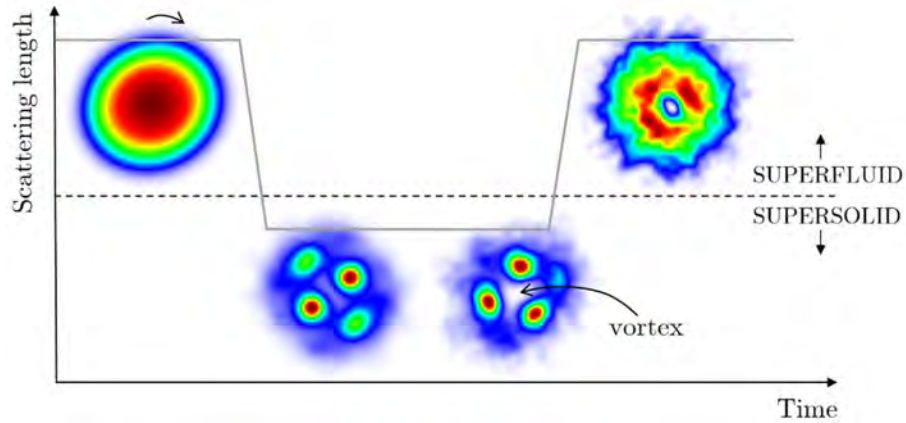

Figure 1. Step-by-step illustration of the protocol process.

REFERENCES
[1] M. Sindik *et al.*, Phys. Rev. A 106, L061303 (2022).
[2] L. Tanzi *et al.*, PRL 122, 130405 (2019).
[3] F. Bottcher *et al.*, Phys. Rev. X 9, 011051 (2019).
[4] L. Chomaz *et al.*, Phys. Rev. X 9, 021012 (2019).
[5] A. Gallemi *et al.*, Phys. Rev. A 102, 023322 (2020).

Creation and robustness of quantized vortices in a dipolar supersolid when crossing the superfluid-to-supersolid transition

M. Šindik,[1,2] **A. Recati**,[1,3] **S. M. Roccuzzo**,[4] **L. Santos**,[5] and **S. Stringari**[1,3]

[1]*INO-CNR BEC Center and Department of Physics, University of Trento, Italy*
[2]*Institute of Physics Belgrade, University of Belgrade, Serbia*
[3]*Trento Institute for Fundamental Physics and Applications, INFN, Italy*
[4]*Kirchhoff-Institute for Physics, Ruprecht-Karl University of Heidelberg, Germany*
[5]*Institute for Theoretical Physics, Leibniz University Hannover, Germany*

Experiments on dipolar Bose-Einstein condensates have recently reported the observation of supersolidity. Although quantized vortices constitute a key probe of superfluidity, their observability in dipolar supersolids is largely prevented by the strong density depletion caused by the formation of droplets. We present a novel approach to the nucleation of vortices and their observation, based on the quenching of the s-wave scattering length across the superfluid-supersolid transition. Starting from a slowly rotating, vortex-free, configuration in the superfluid phase, we predict vortex nucleation as the system enters the supersolid phase, due to the strong reduction of the critical angular velocity in the supersolid. Once a vortex is created, we show that it is robustly preserved when the condensate is brought back to the superfluid phase, where it may be readily observed.

Quantum droplets in dipolar ring-shaped Bose-Einstein condensates

M. Šindik[1], A. Pelster[2] and A. Balaž[1]

[1]*Institute of Physics Belgrade, University of Belgrade, Serbia*
[2]*Department of Physics, Technical University of Kaiserslautern, Germany*
e-mail: marijas@ipb.ac.rs

We study the formation of quantum droplets in dipolar Bose-Einstein condensates in a ring-shaped geometry using numerical techniques. A condensate is initially prepared in a stable ground state of the system, and droplet formation is triggered by a sudden quench of the contact interaction. We investigate how the number of the obtained droplets depend on the total number of atoms in the system, as well as on the strength of the contact and the dipole-dipole interaction. These results can be used in experiments to fine-tune parameters of the system in order to produce droplets of desired size. Furthermore, we study the emergence of supersolidity in the system, when droplets are formed due to the contact interaction quench, but the common phase is still preserved among spatially separated droplets. The quasi-1D geometry imposes additional constraints in the system, in particular when the particle density is higher, such that quantum fluctuation effects become more prominent. We use the Bogoliubov-Popov theory for dipolar Bose systems, including the dipolar analogue of the Lee-Huang-Yang correction, and take into account the condensate depletion due to quantum fluctuations.
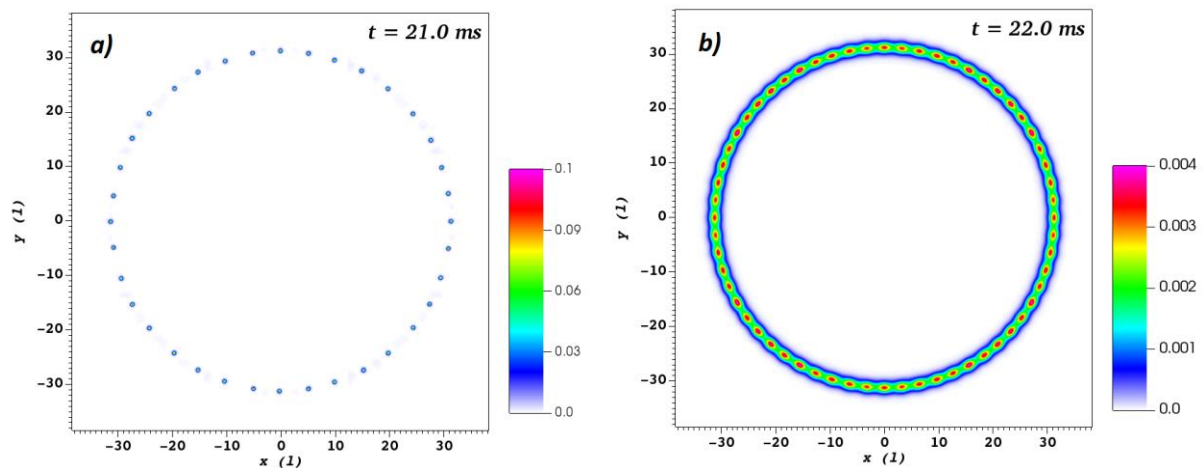
Figure 1. Density distribution in case of a) isolated droplets, b) supersolid state.

Quantum droplets in dipolar Bose-Einstein condensates in a ring potential

M. Šindik[1], A. Pelster[2], and A. Balaž[1]

[1]*Institute of Physics Belgrade, University of Belgrade, Serbia*
[2]*Department of Physics, Technical University of Kaiserslautern, Germany*

We study formation of quantum droplets in dipolar Bose-Einstein condensates in a ring-shaped geometry using numerical techniques. A condensate is initially prepared in a stable ground state of the system, and droplet formation is triggered by a sudden quench of the contact interaction. We investigate how the number of the obtained droplets depend on the total number of atoms in the system, as well as on the strength of the contact and the dipole-dipole interaction. These results can be used in experiments to fine-tune parameters of the system in order to produce droplets of desired size. Furthermore, we study the emergence of supersolidity in the system, when droplets are formed due to the contact interaction quench, but the common phase is still preserved among spatially separated droplets. The quasi-1D geometry imposes additional constraints in the system, in particular when the particle density is higher, such that quantum fluctuation effects become more prominent. We use the Bogoliubov-Popov theory for dipolar Bose systems, including the dipolar analogue of the Lee-Huang-Yang correction, and take into account the condensate depletion due to quantum fluctuations.